https://doi.org/10.5194/egusphere-2026-5567
Preprint. Discussion started: 29 September 2026

Testing the IFU high-spectral-resolution lidar at the 2009 Leipzig field campaign

Thomas Trickl, Helmuth Giehl, Hannes Vogelmann

Karlsruher Institut für Technologie, Institut für Meteorologie und Klimaforschung (IMK-IFU), Kreuzeckbahnstr. 19, 82467 Garmisch-Partenkirchen, Germany

Correspondence to: Dr. Thomas Trickl, thomas@trickl.de, Thomas-Knorr-Str. 47, D-82467 Garmisch-Partenkirchen, Germany; tel. +49-8821-50283; Dr. Hannes Vogelmann, hannes.vogelmann@kit.edu, Karlsruher Institut für Technologie, IMK-IFU, Kreuzeckbahnstr. 19, D-82467 Garmisch-Partenkirchen, Germany; tel.: +49-8821-183-258

Abstract. The mobile three-wavelength aerosol lidar of IFU (Garmisch-Partenkirchen, Germany) was converted into a high-spectral-resolution (HSR) lidar during an extended period ending in May 2009. The system features four simultaneously operated data-acquisition channels, for the backscatter measurements (354.8 nm, 532.2 nm and 1064.4 nm) and for a spectrally filtered second 532.2-nm extinction channel. The system was successfully tested during the EARLINET-ASOS validation field campaign EARLI09 in Leipzig in May 2009, apart from systematic errors in the data that could recently be eliminated in a resumed effort. Here, we compare our results during that campaign with those of the MULIS mobile reference lidar system from the Ludwig-Maximilian University in Munich. The extinction coefficients obtained from the HSR channel and the Raman channel of MULIS agree well (within roughly $\pm 7\times10^{-6}$ m^{-1}) up to vertical distances of about 5 km, with a better near-field behaviour of the HSR caused by analogue detection instead of single-photon counting. In addition, a slightly higher 532.2-nm backscatter signal relative to the Rayleigh background was obtained by the IFU lidar below 3 km. However, there are limitations in the EARLI09 signal quality of the IFU lidar due to problems with the then newly developed 40 MHz transient digitizer that can be greatly improved as known from our other lidar systems. A reasonable daytime performance was found which demonstrates the potentially high value of HSR lidar systems in a lidar network such as EARLINET.

Key words: Lidar, aerosol, extinction coefficients, high spectral resolution, HSRL

1. Introduction

The retrieval of quantitative aerosol extinction coefficients from lidar backscatter measurements has a long history. In the early days this task was solved by the so-called slope method (e.g., Carswell et al., 1972; Kunz and de Leeuw, 1993) that can be, in the absence of Rayleigh backscattering (at long wavelengths), combined with a Klett inversion (Klett, 1981). In the presence of Rayleigh backscattering Fernald (1984) and Klett (1985) provided algorithms including range-dependent particle backscatter-to-extinction ratios $B_P(r)$ that we have named "extended Klett method". For lidar systems with angular scanning capability the slope method can be upgraded by the multi-angle method (Spinhirne et al., 1980; Sasano and Nakane, 1987; Gutkowicz-Krusin, 1993). Here, the data-evaluation effort strongly grows.

Later on, vibrational-rotational Raman backscattering was introduced to obtain aerosol extinction coefficients in a wide spectral range (Ansmann et al., 1990). However, this method is highly insensitive and, therefore, mostly applied during night-time. Rotational Raman scattering provides some gain in sensitivity (e.g., Fig. 9.2 of Wandinger, 2005; Kim and Cha, 2005), also because the returns from both nitrogen and oxygen can be simultaneously used.

https://doi.org/10.5194/egusphere-2026-5567
Preprint. Discussion started: 29 September 2026

Daytime extinction measurements were made possible with the high-spectral-resolution lidar (HSRL) approach that is based on the much more powerful Rayleigh backscattering. Fiocco et al. (1971) gave a first demonstration of a spectrally resolved backscatter signal with a narrow aerosol component residing on a broad molecular return. Shimizu et al. (1983), Shipley et al. (1983) and Sroga et al. (1983) then introduced the HSRL technique. A summary of this technique was given by Eloranta (2005). The elimination of the particle return is achieved by narrowband absorption filters based on atomic (see additionally Alvarez II et al., 1993) or molecular (Piironen and Eloranta, 1994) gases, or interferometry (Grund and Eloranta, 1991). Despite its great potential just a few other lidar teams have built ground-based HSRLs (e.g., Liu et al., 1999; Hayman and Spuler, 2017; Shen et al., 2018). Long-term application of HSRL systems has been more or less restricted to the University of Wisconsin HSRL team (https://www.researchgate.net/scientific-contributions/Edwin-W-Eloranta-2113834593/; e.g., Damoah et al. 2006; de Boer et al., 2009, Volkamer et al., 2015; Reid et al., 2017, to name just a few articles). A few airborne HSRL system have been operated (e.g., Hair et al., 2008; Esselborn et al., 2008). In addition, HSRL could yield a potential for temperature measurements (Hair et al., 2001).

Within the European Aerosol Research Lidar Network (EARLINET, e.g., Amodeo et al., 2006; Pappalardo et al., 2014; http://www.earlinet.org/) the Raman method was chosen as the primary workhorse for extinction retrievals because of its simplicity. This has led to a host of scientific studies that can be found in the publications listed on the EARLINET web site (see above). At the EARLINET station Garmisch-Partenkirchen we preferred the HSRL method since daytime measurements are crucial. On the other hand, due to space limitations in the lidar receiver we just implemented a 532.2-nm HSR channel.

In this paper we describe the system, the mathematical approach and some results from its first thorough testing during the EARLINET-ASOS validation EARLI09 field campaign at TROPOS (Leibnitz-Institut für Troposphärenforschung) in Leipzig (Germany) in May 2009 (Wandinger et al., 2016). During this campaign a total of 11 lidar systems from 9 EARLINET stations were operated on a single site. This offered the unique possibilty of a first comparison of our new HSRL with a number of Raman aerosol lidar systems and we put a lot of effort in finishing the construction of the lidar before that event. Here, we concentrate on a comparison with the side-by-side-operated, proven MULIS (Mobile Multichannel Lidar System) system from the Meteorological Institute of the University of Munich (MIM) that has served as an EARLINET reference system and features a similarly short lower boundary of the operating range.

2. Technical description

2.1 History of the mobile three-wavelength lidar at IFU

Since its delivery by Impulsphysik (Hamburg, Germany) in 1978 the mobile three-wavelength aerosol lidar system of the Fraunhofer-Institut für Atmosphärische Umweltforschung (IFU, Garmisch-Partenkirchen Germany; now: Karlsruher Institut für Technologie, IMK-IFU) has been used in numerous investigations (e.g., Reiter et al. 1979; 1984; Carnuth and Reiter, 1986; Bissonette et al., 1995; Kunz and Trickl, 1996; Hartung et al., 1998; Carnuth and Trickl, 2000; Forster et al., 2001; Kreipl, 2006; Papayannis et al., 2008). Together with the stratospheric lidar (operating range 3 km to more than 35 km (Jäger, 2005)) this system was used at IFU for the routine measurements within the German Lidar Network (1997-2000; Bösenberg et al., 2001) and during the EARLINET project (2000-2002). The mobile system was then operated with two sequentially selected wavelength pairs, (1064.4 nm, 532.2 nm) and (1064.4 nm, 354.8 nm), the short wavelength channels sharing a single photomultiplier tube (Kreipl, 2006). After 2004 the lidar system was gradually converted into a HSRL,

https://doi.org/10.5194/egusphere-2026-5567
Preprint. Discussion started: 29 September 2026

adopting the 532.2-nm iodine-based spectral filtering technique introduced by Piironen and Eloranta (1994). The receiver was not large enough for additional HSR channels. The signals for all three wavelengths were registered after the modification simultaneously as described below.

2.1 Description of the IFU lidar trailer

Figure 1 shows a picture of the lidar trailer taken during the Leipzig field campaign EARLI09. The trailer consists of two compartments, the operating room and the lidar section inside a sliding cover. The cover is pulled back during the operation of the system as seen in Fig. 1. The lidar itself is mounted inside an air-conditioned box that can be tilted in elevation between 0° and 90°, horizontally rotated by ±90° (e.g., Carnuth and Trickl, 2000). Inside the operating room the working desk, the electronics and the computer, the laser power supply, a water cooling system and a small air conditioner used for both the cabinet and the laser compartment. The use of air-cooled water cooling system became necessary after installing a new laser with a 30-Hz repetition rate. The air was exchanged through the two open flaps to the left in Fig. 1.

In Fig. 2 we show an assembly drawing of the lidar box. A new, injection-seeded Nd:YAG laser system was installed (Quanta Ray, model LAB150-30, 0.5 J energy per pulse at 1064.437 nm, 30 Hz repetition rate) in the right half of the laser box (left side in Fig. 1). Due to its higher repetition rate with respect to the 10-Hz laser used earlier shorter measurement times became possible, important for meaningful aerosol sounding under highly variable conditions. The injection seeder (Spectra Physics, model 6350) is directly attached to the L-shaped bar that holds the cavity of the pulsed laser, which ensures an excellent mechanical stability. The first, second and third harmonic outputs of this laser are collinearly emitted into the atmosphere.

A beam fraction of roughly 0.1 % is extracted and further attenuated for the wavelength measurements and for triggering the detection electronics. A few microjoules, spectrally filtered for 532.2 nm, are focussed into a single-mode fibre 8 m long that transfers the light to a wave meter in the electronics rack of the operator compartment (Cluster, model LM007). This type of wave meter had been successfully used for an active wavelength stabilization in our water-vapour differential-absorption lidar (Vogelmann and Trickl, 2008) featuring a measured $\pm 3\times 10^{-8}$ (17 MHz) long-term relative precision and is used here for the same purpose. A second, 0.6-mm-diameter fibre, also 8 m long, is used for transmitting light to the electronics rack where it hits a photodiode serving as the main (ground-free) trigger source. Three more fibres transmit small fractions of the three wavelength radiation components to pulse-energy monitors. The calibration of the wave meter was routinely verified by measuring the centre of the gain range of a broadband HeNe laser near 632.991395 nm (Schweitzer et al., 1973), by watching the full frequency range of the thermally drifting reference laser.

The laser cabinet inside the lidar box is temperature stabilized by using a heater and controlled inflow of cooled air from the air-conditioner in the operator compartment fed into the box through a large hose. The metal pipe of the heater was originally installed at the bottom of the lidar box in order to keep the optics dry during field operation of the system under moist conditions.

The receiver optics are mounted in a separate cabinet inside the lidar box. An f = 2.3 m telescope with 0.30 m diameter is used to collect the backscattered light. In contrast to the other IFU lidars a Cassegrain telescope was chosen in order to reduce the space requirement in the small receiver box. An iris aperture with electronically controlled shutter is placed in the focal plane of the telescope. The receiver optics and the detectors are positioned as shown in Fig. 3. The laser beam is aligned by watching its far atmospheric spot in the telescope image through a hole in the rear plate of the receiver without optics. We follow the strategies described by Vogelmann (2008) and Trickl et al. (2020), applying a 4-f relay optical design, imaging the primary mirror of the

https://doi.org/10.5194/egusphere-2026-5567
Preprint. Discussion started: 29 September 2026

telescope on the filters and detectors in order to minimize an influence of surface inhomogeneity and the diameter of the radiation bundle.

Beam splitters with almost perfect selectivity and polarization-independent coatings were custom-made by Laseroptik (Garbsen, Germany), accounting for the different polarizations of the spectral components of the laser beam. The back sides of the optics were anti-reflection coated, also the lenses in order to reduce the influence of the surface curvature on the transmittance. The final wavelength selection and daylight suppression is done with three interference filters with 0.5 nm spectral width at half maximum and 1″ diameter (Barr Associates), each placed in exit pupils of the telescope. The beam is expanded to the full width available inside the Barr filters which results in a full overlap of laser beam and telescope field of view at distances of about 180 m. No optical surfaces are close to focal points. Because of the space limitations optics holders were chosen that can be aligned from above (Radiant Dyes).

Two glas cells filled with iodine vapour were installed in the HSR channel as depicted in Fig. 3. By using two cells we could almost maximize the absorption path. The cells were heated by two heating tapes (manufacturer) with maximum permitted temperature of 100 C. We carefully stepwise enhanced the cell temperature until, by the end of the field campaign, no contribution from cirrus clouds was left in the HSR backscatter signal. A spectral filter behind the cells should be considered to minimize the spectrally widely distributed iodine fluorescence. This is a problem for the short-lived fluorescence of alkali vapours, but should be small because the long fluorescence life time of I_2. of roughly 1 µs (e.g., Capelle and Broida, 1973). By tuning the laser frequency outside the iodine spectral line we verified that the two 532.2-nm backscatter signals could be made identical by adjusting the supply voltage of the photomultiplier tubes (PMTs).

Three Hamamatsu P7400U-04 PMTs with actively stabilized dynode voltages and a large-size pin photodiode with integrated pre-amplifier (ME30FK-V4D-PD) serve as the detectors, all supplied by Romanski Sensor- und Verstärkertechnik (RSV) and optimized for this lidar (Kreipl, 2006). The photodiode was very successfully quality assured by Freudenthaler in the late 1990s (V. Freudenthaler, presentation within the German Lidar Network (Bösenberg et al., 2001)). Also the detectors were placed in exit pupils in order to avoid an influence of the inhomogeneous cathode structure. Ground-free PC-controllable detector power supplies are used (Ingenieurbüro W. Funk). The reference voltage was taken from a 5-V module on each PMT socket and transmitted to the respective power supply for generating the adjustable operating voltage. In this way, an initially observed undershoot of the lidar signal could be removed (Fig. 3.12 of Kreipl, 2020). Signal-induced nonlinearities (e.g., Bristow et al., 1996) at the very high radiation levels in the HSRL receiver are avoided by keeping the signal below 40 mV (into 50 Ω). This required to operate the PMTs with supply voltages around just 450 V (Fig. 3.10 of Kreipl, 2006, available at http://www.trickl.de/PMT.PDF). At 450 V the relative gain in the HSRL channels is approximately 0.014 with respect to that at the normally recommended 800 V (see Fig. 10 of Trickl et al., 2020).

The signals from all four detectors were amplified with highly linear (Trickl et al., 2020) adjustable-gain preamplifiers (Analog Modules, model 351A-1, inverting version for the amplification of the signal from the photodiode) in order to allow operating the transient digitizers in their least-noisy 500 mV range. A four-channel transient digitizer system is used (Licel, 12 bit, 40 MHz). Given the excellent experience with the low-noise Licel 20 MHz system since 1996 (Trickl et al., 2020; 2024; 2025; Klanner et al., 2021) this step towards a completely new instrument was somewhat risky, which is confirmed in the measurements presented in Sect. 3.

During EARLI09 the HSRL was operated at an elevation angle of 85 degrees in order to reduce the effect of near-specular reflection by ice crystals.

https://doi.org/10.5194/egusphere-2026-5567
Preprint. Discussion started: 29 September 2026

2.2 MIM lidar trailer

The Mobile Multichannel Lidar System (MULIS) was operated by MIM during EARLI09 within a distance of less than 10 m from the IFU trailer. MULIS has been used as a primary EARLINET reference system and has validated numerous EARLINET lidar systems all over Europe (e.g., Freudenthaler et al., 2010; Pappalardo et al., 2014; Wandinger et al., 2016). Thus, we see a comparison with this lidar as an excellent choice.

A brief description of MULIS was given by Freudenthaler et al. (2009). MULIS is a five-wavelength lidar system with backscatter channels at 354.8, 532.2 and 1064.4 nm and nitrogen Raman channels at 387.8 and 607.5 nm. The emission of the Nd:YAG laser (Continuum, Surelite II, 10 Hz repetition rate) is frequency doubled and tripled by means of KD*P (potassium dideuterium phosphate) crystals, and the output at 532.2 nm is assumed to be perfectly linear polarized, which is needed for accurate measurements of the depolarization of the backscattered radiation including the calibration. An adjustable field stop is used to decrease the field of view to limit the maximum signal to an acceptable level. This tilted-slit aperture accounts for the longitudinal walk of the focus as a function of distance r (Freudenthaler, 2003). To minimize diattenuation and polarization effects of the dichroic beam splitters, all optical coatings are custom-designed (Laseroptik, Germany).

As in the HSRL, the detectors in the 532 nm depolarization channels were Hamamatsu R7400U-04 PMTs with actively stabilized dynode voltages supplied by RSV. For preamplification and analog-to-digital conversion (ADC) two transient recorders from Spectrum GmbH, Germany, were used, i.e. model PCI.412 with 12 bit resolution for the parallel and the MI.4022 with 14 bit resolution for the cross polarization signal; both at 20 MHz sampling rate. The preamplifier stages of the ADC-boards were custom optimized regarding signal linearity using a custom made lidar signal pulse generator (LISIG) with the aim to minimize signal distortions in the clean, free troposphere (Freudenthaler, et al., 2018). Due to the weak Raman backscatter signals photon counting detection was applied in the Raman channels using a Licel R7400-U20 PMT module at 607 nm with a Licel PR20-160-P photon counter. The sensitivity of individual channels were adjusted with absorbing neutral-density filters (Schott).

2.2 The IFU HSR mathematical approach

For the inversion of the HSR data channel, the spectral information deleted by the filtering in iodine vapour must be resynthesized by computing the Rayleigh-Brillouin line profile and its gap caused by the iodine filter. The full Rayleigh-Brillouin line shape, as described in Forkey´s thesis (1996), was first approximated as a sum of three Voigt lines, which was driven by the shape of the far wings (Trickl and Giehl, 2010). For an example see Fig. 4. The normalized parameters X and Y in this figure are defined as specified by Forkey (1996). X = 1 corresponds to half the 1/e width of a pure Doppler line, i. e., 1.2011 times the full width at half maximum:

$$\Delta\nu = \lambda^{-1}\sqrt{\frac{8kT}{m}}\,, \qquad (1)$$

m = 28.9522 u (air mass unit, U.S. Standard Atmosphere, 1976).

The Y parameter is approximated by Forkey as (assuming pure backscattering here):

$$Y = 0.230\ \frac{T\ [K] + 111\ K}{(T\ [K])^2}\, P\ [atm]\ \lambda\ [nm]\,. \qquad (2)$$

For P = 1 atm (1013.25 mbar) and T = 300 K Y = 0.559. Y is a parameter in the Tenti S6 model applied by Forkey (Tenti et al., 1974). It is mentioned here to label the spectra in Forkey´s Fig. 2.5 (Y = 0.5, 1.0, 2.0 and

https://doi.org/10.5194/egusphere-2026-5567
Preprint. Discussion started: 29 September 2026

5.0) that were digitized for the Voigt approximations made. The Voigt parameters for the four spectra were interpolated by spline curves allowing us to generate spectra for intermediate Y values.

However, later on, Witschas (2011a,b) provided a considerably simpler approach with a similar performance for calculating the Rayleigh-Brillouin line triplet based on three Gaussian lines from air temperature and pressure, i.e., from the parameters X and Y. These formulae are much easier to implement in a computer program than the Voigt approach. A comparison of calculations with this approach with the Y = 0.5 exact line from Forkey (1996) is shown in Fig. 5, together with a line synthesized for T = 300 K and P = 1000 mbar (Y = 0.5596. Because of the excellent agreement, we decided to use the Witschas procedure for the evaluations after 2011, in a preliminary version obtained from the author that yielded almost identical results.

The Doppler-broadened hyperfine absorption spectrum of I_2 was calculated by using the IodineSpec4 program (Toptica) (Bodermann et al., 2002; Knöckel et al., 2004), after very successfully testing with spectroscopic data (Trickl et al., 2007). The program is based on precision laser spectroscopy (Veltchev et al., 1998; Xu et al., 2000) and provides a quoted 2σ uncertainty of calculated iodine frequencies of ±3 MHz (±0.0001 cm^{-1}) between 526 nm and 667 nm, including the hyperfine splitting. In Fig. 6, we show a calculation for 340 K for both a narrow laser bandwidth and a line width for typical ambient conditions. The iodine transition peaking at 18789.2770 cm^{-1} was chosen that is closest to the optimum frequency of the laser. This line also does not overlap with strong neigbouring lines which reduces uncertainties caused by changes in the I_2 cell temperature.

The line widths depend mostly on the extension of the hyperfine splitting (see red curve) which can be expected to minimize in the case of angular momentum J = 0 because of the absence of a quadrupole splitting. The selected line has an acceptable width of 1.394 GHz. A nearby line at 18789.667 cm^{-1} is even thinner (0.0275 cm^{-1} or 0.824 GHz for 38 % absorption), but was not taken because of potential incomplete absorption under our heating conditions.

The overall line shapes calculated from the Witschas (2011a, b) algorithm (for Y = 0.5) and the IodineSpec4 absorption spectrum rescaled by multiplying with four different factors is presented in Fig. 7. It is obvious that the area of the transmitted line does not change much as a function of the scaling factor of the line strength. This is confirmed in Fig. 8 for temperatures and pressures from a radiosonde ascent at IfT (Leipzig) on 25 May 2009, 21:15 CET (Central European Time, = UTC + 1 h), during the main period of the EARLI09 comparisons. In Fig. 8 the spectral area ratio *f(r)* between iodine-depleted and the full spectral distribution of the backscatter signal is shown for three different absorption strengths of iodine. These absorption strengths are calculated by multiplying the IodineSpec4 output around 18789.2770 cm^{-1} with scaling factors of 10000, 20000, 25000 and 30000, respectively, and by applying Beer and Lambert´s law. For the factor 10000, the absorption is incomplete (see Fig. 7). A factor of 20000 is close to the final situation achieved after gradually enhancing the temperature of the iodine cells and was, therefore, chosen for the retrieval. A sensitivity study showed that *f(r)* is not affected by laser frequency variations in the vicinity of the iodine line centre.

When normalizing the highest value of *f(r)* to 1 (upper part of Fig. 8) it is even more obvious that, apart from the not relevant case of the factor 10000, the influence of the iodine line strength is not critical. Thus, its influence on the uncertainty of the slope and the retrieved extinction coefficients is small.

The particle extinction coefficient at distance r_i is obtained by solving the lidar equation for the HSR channel, considering that

$$\frac{d}{dr}\ln y = \frac{1}{y}\frac{d}{dr}y .$$

https://doi.org/10.5194/egusphere-2026-5567
Preprint. Discussion started: 29 September 2026

The derivative is formed by a linear least-squares fit, and this transformation removes the asymmetry of the data noise of the logarithm at low values of y required for the fitting procedure. Following Vogelmann and Trickl (2008) and Trickl et al. (2020) we obtain the particle extinction coefficient

$$\alpha_P(r_i) = \frac{1.5}{\Delta r\ y_i} \frac{\sum_{j=i-k}^{i+k}(j-i)y_j}{k(k+1)(2k+1)} - \alpha_R(r_i), \tag{3}$$

at data bin *i*, with the Rayleigh extinction coefficient α_R (calculated from radiosonde data as described by Trickl et al. (2024)) and

$$y_i = \frac{r_i^2 S_{HSR}(r_i)}{f(r_i)\beta_R(r_i)}. \tag{4}$$

S_{HSR} is the backscatter signal in the HSR channel, $f(r_i)$ the spectral area ratio and $\beta_R(r_i)$ the Rayleigh backscatter coefficient at distance r_i. k = 14 was chosen for Eq. 3. The Rayleigh extinction and backscatter coefficients are calculated from the atmospheric density (see below).
The particle backscatter coefficients are obtained from the lidar equation by inserting the particle extinction coefficients from Eq. 3. In addition, an extended-Klett solution for β_P is provided (Klett, 1985). In both cases a reference value must be provided for calibration which may add uncertainty.
The HSR raw signal was smoothed with a Blackman-type numerical filter as described by Trickl et al. (2000) covering 2×*k*+1 data points. By selecting *k* = 14 the small-scale digital noise of the signal was removed (see Sect. 4).

After applying Eq. 3 the particle extinction coefficient is also smoothed. The filtering half interval is dynamically increased with the distance above the lidar to account for the growing noise, based on the formula

$$k = a + b \times i + c \times i^2 \tag{5}$$

for bin *i* (for values see Sect. 4). The quadratic term was chosen to compensate the quadratic growth of the noise of the range-corrected signal (Eq. 4). The range resolution in the VDI definition (VDI, 1999), introduced by C. Weitkamp, is then obtained from 0.192×2×k×Δr, Δr = 3.7475 m, as described by Trickl et al. (2020). Other definitions are given by Iarlori et al. (2015) and Leblanc et al. (2016), see Sect. 5 in (Trickl et al., 2020).
In the examples shown in this paper the atmospheric number density and we calculated the Rayleigh backscatter and extinction coefficients from the data of Vaisala RS92 radiosonde ascents, based on the highly accurate algorithm provided by Owens (1967). The launches of the sondes were carried out in the front of the TROPOS institute building (51.35 N, 12.43 E, 117 m a.s.l.) during each measurement period of the EARLI09 field campaign. For deriving the backward and total optical coefficients we follow the physical background provided by She (2001), taking into account the 0.5-nm full spectral width at half maximum of the interference filters (Trickl et al., 2024). We assume a relative uncertainty of the obtained coefficient of about 0.5 %. In this way the influence of the small Rayleigh backscatter and extinction coefficients on the retrievals is negligible. The noise is just determined by the signal noise in the HSR channel. In the absence of radiosonde data, the two-signal approach of Eloranta (2005) could be applied which requires system modifications (Sect. 5). Here, the noise is influenced by that of both 532.2-nm channels. Alternatively, approximations of the atmospheric density can be used.
Particle backscatter coefficients are calculated by both inserting the evaluated extinction coefficients into the lidar equation and applying the extended Klett inversion (Klett, 1985; see also Speidel and Vogelmann, 2023).

https://doi.org/10.5194/egusphere-2026-5567
Preprint. Discussion started: 29 September 2026

The IFU Klett algorithm contains variable backscatter-to-extinction ratios in ten selectable layers or with external lidar ratios. It very successfully passed the EARLINET quality-assurance programme (e.g., Böckmann et al., 2004) in the final phase and was, again, refined including details of the rotational Raman spectrum and ozone corrections (Trickl et al., 2024). The ozone correction for 532.2 nm is not applied here since it is relevant only in the stratosphere. Both approaches for calculating the backscatter coefficients require to provide reference a reference value which, in the presence of noise, is a source of uncertainty and, thus, must be made with care in a range without aerosol identified from the measurements at 1064.4 nm. Such a range existed during the periods discussed here.

4. Results

4.1 Lidar performance during the Leipzig field campaign 2009

During the EARLI09 Leipzig field campaign (Wandinger et al., 2016) the performance of the just completed HSRL could be determined in detail for the first time. We operated the lidar during the Leipzig campaign between May 18 and May 27, 2009, and acquired roughly 1500 one-minute measurements in all four data-acquisition channels.

The greatest positive surprise was that the wave-number noise of the laser indicated by the LM007 wave meter was just ±0.0002 cm^{-1} (±6 MHz), despite the strong vibrations of the trailer caused by the laser cooling unit. A small thermal drift was observed, particularly at outside temperatures above 24° C at which the internal cooling was unable to follow the temperature rise. The typical thermal drift of the laser frequency was 0.002 cm^{-1} h^{-1} and was compensated by manual adjustments every half an hour.

As mentioned we realized that the first exclusively used short iodine cell could not be heated enough because of the 100º C maximum temperature allowed for the heating tape. Therefore, a second, longer I_2 cell was added in the section around the focal point. The second cell, still, was not sufficient and was, therefore, heated with a current supply borrowed from TROPOS on the final day of the campaign: On 26 May the strong backscatter signal from a cloud was completely absent in the HSR channel.

For the comparison of all 11 lidar systems participating the night-time period between 22:00 and 24:00 CET (Central European Time = UTC + 1 h) on May 25 was selected. The choice of night hours was dictated by the need to validate the rotational-vibrational Raman channels. The backscatter profiles for all 1-min measurements within these 2 h were summed up. We also examined 15-min averages and found considerable variability in the aerosol-related structure. The extremely long averaging helped us to detect quite surprisingly systematic structures in the HSRL backscatter data (see next section).

4.2 Data corrections

As mentioned above, the data evaluations for the common publication (Wandinger et al., 2016) revealed issues with the data quality of the transient digitizer system. In contrast to the extremely low noise of the 20-MHz transient digitizers of Licel (Trickl et al., 2020) the new 40-MHz system generated strange, coherent patterns that could be analysed because of the 2-h averaging demanded for the community test case (25 May 2009, 22 to 24 CET).

The data noise consisted of groups of repetitive 2^n bins differing in signal with respect to the groups of bins between them. The most important groups in both 532.2-nm channels were 4 and 8 bins long. This structure

https://doi.org/10.5194/egusphere-2026-5567
Preprint. Discussion started: 29 September 2026

could be easily removed by data smoothing as pointed out in Sect. 2.2. In the HSR channel (channel 3) pronounced 2028-bin and small 256-bin structures were additionally present and mathematically corrected. The unfiltered 532.2-nm channel (channel 2) as well as the 354.8-nm and 1064.4-nm channels did not exhibit anything similar although the low-signal regions did not look perfect. As a first step in the HSR retrieval algorithm the raw data were just smoothed with the ±14-bin sliding Blackman filter. In graphical presentations of the raw data ±15-bin sliding arithmetic averages were made.

It should be mentioned that perfectly performing 40-MHz transient digitizers (also without any signal-induced wings) are meanwhile available from Licel, one system being used since 2025 in our stratospheric aerosol lidar system (Trickl et al., 2024).

The backscatter profiles of the HSRL showed a good near-field performance down to distances just above the peak signal at 0.18 km. However, in all four detection channels a tiny signal distortion with amplitude of about 2×10^{-5} relative to the peak signal) were detected that formed a broad hump around the tropopause. The hump could be perfectly removed by subtracting a broad Gaussian curve, comparing the result with simulated Rayleigh signals calibrated in aerosol-free ranges. As we know from earlier experience (Trickl, 2010) the distortion was very likely caused by to the magnetic field of the laser flashlamps. This small effect could not be visually detected during the measurements. From experience gained over the years (Trickl et al., 2020) we see connecting the preamplifier zero voltage as the most likely reason.

Another issue was a slight ringing observed on the first 1.5 km. This small effect was meanwhile admitted by Licel and ascribed to problems with the anti-aliasing filter in these new transient digitizers. We attempted a correction that yielded a more reasonable result, but did not remove the uncertainty.

Finally, on 25 May a residual aerosol backscatter component was found in the HSR data (channel 3). This effect was not adequately treated in the data submitted for the work underlying the publication of Wandinger et al. (2016). It was now removed by calculating the aerosol component in the unfiltered 532.2-nm channel (channel 2) alone, subtracting the corresponding simulated Rayleigh curve. The residual cirrus signal in channel 2 around 12 km disappeared by subtracting 13 % of this aerosol component. This correction yielded satisfactory results as shown below.

No such aerosol correction was needed for the data on 26 May when the iodine cells were sufficiently heated to reach 100 % absorption. However, these daytime measurements are not included in the EARLI09 comparison of the extinction channels because of the low sensitivity of the Raman channels.

4.3 Results for the common comparison case 25 May 2009, 22:00 to 24:00 CET

Figure 9 summarizes the range-corrected backscatter profiles of the HSRL for all three laser wavelengths, together with simulated Rayleigh profiles adjusted to the backscatter signals in the range below the cirrus cloud between 11.0 and 12.9 km. The cirrus cloud ends just below the tropopause (12.98 km after correcting the geopotential altitudes of the radiosonde) which is a well-known behaviour in almost three decades of ozone measurements (Carnuth et al., 2002, to Trickl et al., 2020). The tropopause is defined here not by the first major change in the temperature lapse rate, but by the temperature minimum closest to the final drop of the relative humidity.

Apart from the 4- and 8-bin structures the digital ripple in the data of channels 1, 2, and 4 is less pronounced than that in the HSR channel (channel 3). In the stratosphere the artificial structure is increasingly amplified by

https://doi.org/10.5194/egusphere-2026-5567
Preprint. Discussion started: 29 September 2026

the range correction. Minor corrections were made in channel 2 justified by the comparisons for 532 nm. In Fig. 9b also the corresponding range-corrected backscatter profile of MULIS is shown for comparison. Below 2.6 km there is a discrepancy that grows towards the ground. This is also the case for several 532-nm raw-data profiles from the other participants (Fig. 4a of Wandinger et al., 2016). Because of the extremely careful alignment of the HSRL polychromator we have problems to assume signal nonlinearity in HSRL channel 2 at short distances. However, the short distance between the laser beam and the detection axis is known to yield quite easily near-field signal overshoot (Sect. 4.2.1 of Trickl et al., 2020). A four-quadrant ("telecover") test (Freudenthaler, 2008) would have been needed for a clarification and the quadrant on the laser side could be blocked (Trickl et al., 2020). On the other hand the HSRL had the best near-field overlap, with signal peaks at about 150 m (here: slightly higher due to the range correction). Thus, problems of the EARLINET lidar systems exhibiting less signal below 2.6 km cannot be excluded. The discussion of this issue will be resumed when presenting the lidar ratios further below.

As mentioned, 15-min averages were made for the entire period that show a considerable variability of the aerosol distribution and the cirrus cloud. This demonstrates that short measurements periods are necessary below the capability of many Raman lidar systems.

From the 1064.4-nm backscatter profile we conclude that the tropospheric aerosol ends at a distance of 6.3 km above the lidar site. This disagrees with the 532.2-nm evaluations of a number of the participating lidar systems that show aerosol in this range, also for MULIS (Wandinger et al., 2016). Thus, the MULIS 532.2-nm backscatter coefficients were re-evaluated with better reference values, with both the Raman-based and the Klett inversions.

Figure 10 shows the range-corrected HSR signal after removing the systematic structures. The short-scale digital noise in the HSR data is nicely smoothed away with a sliding ±15-bin arithmetic average (±56 m, corresponding to VDI range resolution of 56 m (VDI, 1999); see (Trickl et al., 2020)). In the upper panel the refined signal is shown up to 20 km, revealing good agreement with a Rayleigh simulation, apart from growing ripple of the smoothed signal above 10 km. Around 12 km the slope change due to the extinction of the radiation by the cloud is seen. Below r = 6.3 km the signal starts to depart from the Rayleigh simulation.

The lower panel of Fig. 10 displays a magnified section of the upper panel. In addition, the range-corrected signal of the MULIS Raman channel (607.5 nm) is given for comparison. The two profiles agree down to 1.2 km where the MULIS overlap function starts to deteriorate because of the use of photon counting in this channel. This looks remarkable considering the differing wavelengths, but the influence of the Ångström exponent on the Raman retrieval is just a few per cent for moderate values (Ansmann and Müller, 2005).

Figure 11 shows the particle extinction coefficients obtained for the EARLI09 test case from both lidar systems. The HSRL results are somewhat uncertain up to 2 km due to the estimated ringing correction. The residual noise above 2 km is amplified by the range correction. Thus, a Blackman filter with growing interval size was applied ($a = 20$, $b = 0.03$, $c = 7\times10^{-5}$ in Eq. 5). The resulting VDI range resolution is also shown in Fig. 11 (red curve).

The HSR retrieval (Fig. 11) is highly sensitive to the slope of the signal and, thus, yields reasonable extinction coefficients not before 0.4 km. The hump in the signal below 0.4 km (Fig. 10) had been absent during the optical alignment on the previous day and must be ascribed to an increase of particles in the lowest layer above the ground. Unfortunately, we did not consider a measurement at low elevation angle in order to determine the extinction coefficients in this layer.

https://doi.org/10.5194/egusphere-2026-5567
Preprint. Discussion started: 29 September 2026

The HSR extinction coefficients agree rather well with those from MULIS (adopted from Wandinger et al., 2016) apart from the range below 2 km where the influence of the overlapping photon pulses started in the MULIS 607.5-nm profile. We also compare the HSR result with 50 sr times the backscatter coefficients obtained by inserting the extinction coefficients into the lidar equation (Fig. 12). The agreement is slightly less good, but it allows us to judge the quality of the HSR extinction coefficients below 1.5 km. In any case, the agreement with MULIS ($\pm 7\times10^{-6}$ m^{-1}) is better than that with the other EARLI09 participating systems: Figure 6 of Wandinger et al. (2016) shows a considerable system-to-system variability of the particle extinction coefficients. Given the above differences with respect to MULIS we estimate the uncertainty to $\pm 1\times10^{-5}$ m^{-1}, perhaps more below r = 1.5 km.

Extinction coefficients of 1×10^{-4} m^{-1} mean a reduced visual range of about 39 km assuming a 2 % contrast limit in Koschmieder´s (1925a; 1925b) theory. A lower visual range is expected within the lowest few hundred metres.

We also derived backscatter coefficients β_P necessary for calculating the lidar ratios, for both the HSRL and MULIS (Fig. 12). As mentioned, for MULIS, now the aerosol-free range above 6.3 km was now used as the reference. As expected from Fig. 9 the peak β_P from MULIS are smaller than those from channel 3 of the HSRL. A lidar ratio of 50 sr (i.e., a Klett-type B_P = 0.020 sr^{-1}) yields a reasonable agreement with the extinction-based evaluation. Bp = 0.015 sr^{-1} leads to lower backscatter coefficients.

Finally, we give in Fig. 13 a comparison of the 532-nm lidar ratios obtained for both lidar systems. In both cases the backscatter coefficients for the extinction method were taken. The useful range of the HSRL is limited to the range between 0.7 and 3.5 km. For more reliable results at larger distances a separate far-field detection channel would be needed. Despite the considerable uncertainty of the signal corrections below 2 km the lidar ratios of the HSRL stay in a reasonable range there. As to the high-signal issues discussed above we conclude that near-field signal distortions should be approximately the same in all four detection channels. Thus, a partial compensation of errors could be the case similar to a differential-absorption lidar.

4.4. Daytime performance: 26 May 2009

In the morning of 26 May an enhanced particle level was visually observed leading to the idea of Saharan dust for the preceding night and the morning. The final observation period of EARLI09 took place between 9:00 and 11:00 CET. The HSRL was operated for start times between 10:01 and 11:58 CET. The observational period was characterized by occasional cloud interference below 7 km (Fig. 14) and an up to four times higher daylight background. During the cloud phase between 11:00 and 11:15 CET also stronger levels of the presumable dust was registered (e.g., r = 2.5 and 3 km in Fig. 14). As revealed by inspection of the 1-min individual measurement, also the aerosol distribution changed on a short time scale.

Figure 14 demonstrates the absence of particle backscatter contributions in the HSR profiles on 26 May verifying that the mentioned additional heating of the second iodine cell was successful. The cloud peak at 5.8 km in the one-minute HSR backscatter profile at 11:14 CET is about 100 times higher than the backscatter signal below the cloud, but no cloud influence can be discerned in channel 3.

For the extinction retrievals we averaged the data over 15 min. We focus here on two cloud-free 15-min periods. The digital ripple and the magnetic interference of the laser flashlamps were corrected as in the case of the data from the preceding night. Both, measurements 30 to 44 (start times 10:31 to 10:46 CET) and measurements 90 to

https://doi.org/10.5194/egusphere-2026-5567
Preprint. Discussion started: 29 September 2026

104 (11:31 to 11:46 CET), yielded relatively reasonable results (Figs. 15 and 16). Due to the solar background the related background noise level is slightly higher. This and the shorter averaging time may be the reason for the slightly higher vertical variability of the extinction coefficients as compared with the case in Sect. 4.3. From the oscillations we estimate the uncertainty in the range with aerosol to roughly $\pm 1.5\times10^{-5}$ m^{-1}.

The noise considerably affects the retrieval of the backscatter coefficients of both the direct and the Klett inversion because of the more problematic determination of the effective reference value. This can influence the quality of the lidar ratio. Again, the signal corrections mentioned for the preceding night were made with great care for the HSR channel.

The lidar ratios are lower than expected from typical values. However, at least the second case (Fig. 16) elevated values were obtained in the ranges of the two aerosol peaks. The downward shift of the average lidar ratios could reflect the uncertainty of the measurement in this technical state of the system, but also potential mixing with other air masses (see Sect. 5). We conclude that with technical improvements high-quality measurements will be possible during both daytime and night-time.

5. Discussion and Conclusions

The upgraded three-wavelength aerosol lidar was successfully tested during the Leipzig field campaign in May 2009. The technical performance is satisfactory, apart from the slight thermal drift of the laser frequency. The problem with the heating of the iodine cell was gradually solved, avoiding to damage the heating tapes wrapped around the cells (maximum rating 100 ºC). The main limitation by the quality the transient digitizer has been meanwhile solved by the manufacturer. Even the very small signal-induced exponential wings (Trickl et al., 2020; 2024) no longer exist in the most recent models.

In order to extend the operating range, a separate far-field channel must be installed: Given the huge peak backscatter radiation level there is sufficient PMT gain reserve for achieving high signals in the entire troposphere after strongly reducing the near-field contribution. The far-field operation must be made sequentially in time because of the space limitations in the receiver box. This can be done by switching the input aperture size of the polychromaztor at fixed time intervals. This adjustment requires a motorized razor blade. At the same time the PMT voltage must be switched.

The design must be made with care since the solar-background contribution in the signal must be kept below 1 mV in order to avoid electronic deformation of the lidar backscatter signal (Trickl et al., 2020). In the near-field operation, due to the limitation of the peak signal and the extreme drop in signal with distance the solar background was much lower than the 1-mV level. This can be quite different if a high signal is admitted in a far-field mode of operation. Here, the background can exceed the 1-mV limit.

Finally, a computer-controlled tuning unit for the seed laser is desirable. In this way not only an automatic wavelength stabilization can be achieved, also the application of the calibration procedure by wavelength tuning described by Eloranta (2005) becomes possible. An interesting frequency-stabilization approach involving stimulated Brillouin scattering was chosen by Eloranta and Razenkov (2006). However, given the positive experience with our water-vapour lidar (Vogelmann and Trickl, 2008) we plan to stay with a frequency control by the wavemeter. In this way the laser frequency can be directly visualized.

As can be seen in Fig. 6 of Wandinger et al. (2016) the scatter of the extinction coefficients of the participating lidar system is quite remarkable with consequences for the quality of the lidar ratios. Our results, after the necessary data corrections, agree best with those for the MULIS system.

https://doi.org/10.5194/egusphere-2026-5567
Preprint. Discussion started: 29 September 2026

Measurement times of 15 min are enough for retrieving extinction coefficients with substantial quality during daytime and are expected to shorten after eliminating the digital noise. Not all measurements on 26 May were useful because of occasional cloud interference below 6 km (Fig. 14). Also the dust load changed and passed a maximum during the period just after 11 CET. In the future Nd:YAG lasers with 100-Hz repetition rate or more will be used (see Trickl et al., 2024) and will further shorten the measurement time for physically meaningful measurements in the presence of transient aerosol or cloud layers.

No photon counting was applied at that time because of our excellent previous experience with the 20-MHz transient digitizers of Licel. Photon counting makes sense just during night-time, but then yields significantly lower noise levels for sufficiently long averaging (Trickl et al., 2024).

The lidar ratios on both days are slightly lower than expected from the literature. This was also the case for MULIS. Mostly, values between 40 sr and 50 sr prevail. 50 sr was established as the EARLINET average (Pappalardo, 2003). A list of source-specific lidar ratios was published by Müller et al. (2007). Just for marine aerosol values clearly below 50 sr were listed (about 25 sr). This means a mixture with marine aerosol must be considered to explain lidar ratios strongly below the "standard" value.

Accidentally, as suspected, the final two days of EARLI09 overlapped with a Saharan-dust period. Saharan dust cases have been extensively studied with lidar (e.g., Jäger et al., 1988; Carnuth et al., 2002; Papayannis et al., 2008). The EARLINET publication list (https://www.earlinet.org/) contains numerous articles devoted to Saharan dust and its optical properties, starting with (Ansmann et al., 2003; Müller et al., 2003; Balis et al., 2004). Systematic investigations of lidar ratios of Saharan dust after long-range transport were published by Mamouri et al., (2013), Groß et al. (2015) or (Nisantzi et al., 2015; Papanikolaou et al., 2024). Higher lidar ratios of the order of 55 sr are reported to originate from western North Africa, values below 50 sr more from the east.

In order to analyse the atmospheric situation we calculated backward trajectories with the HYSPLIT model (https://www.ready.noaa.gov/HYSPLIT_traj.php, Draxler and Hess, 1998; Stein et al., 2015). Four examples are shown in Fig. 17. During the late hours of 25 May the trajectories initiated at low altitudes indicate transport times of 13 days and more from North Africa to Leipzig. We see contributions from rather different source regions which suggests considerable mixing of air different types of aerosol, possibly even marine particles. Just in the altitude range around the peak between 1.2 and 2.8 km Saharan air masses arrived rather directly. In the morning of 26 May, the aerosol level is higher and the trajectories demonstrate more contributions from North Africa. In the case of Fig. 16 somewhat elevated lidar ratios were obtained in the ranges of the two aerosol humps around 2.6 and 3.6 km. However, fully trustable lidar ratios require the planned technical upgrading. We expect a considerable improvement with respect to Raman lidar systems.

5 Data availability

The EARLI09 data from the IFU and MIM lidar systems can be obtained from the authors or Volker Freudenthaler if there is a well-specified purpose. In general, the campaign data have been internally archived for the EARLINET validation purpose.

6 Author statement

TT and HG developed the system and carried out the measurements. TT evaluated the HSRL data. All authors contributed to preparing this manuscript.

https://doi.org/10.5194/egusphere-2026-5567
Preprint. Discussion started: 29 September 2026

7 Competing interests

The authors declare that they have no conflict of interest.

Acknowledgements

The authors thank Wolfgang Seiler and Hans Peter Schmidt for their support, Albert Ansmann, Edwin Eloranta, Oliver Reitebuch and Benjamin Witschas for the intense and valuable discussions. Volker Freudenthaler provided the MULIS data, reviewed and upgraded the description of the MULIS lidar system, however renouncing a co-authorship. Ulla Wandinger and Holger Baars made available additional data of the EARLI09 comparison (Wandinger et al., 2016). Josef Burger made great contributions to the general modifications of the lidar trailer, especially concerning the laser cooling approach. The authors are indebted to Werner Funk, Bernd Mielke, Heinz Josef Romanski and Bernhard Stein for numerous important discussions and technical solutions for the detection electronics.Werner Fuß helped us with filling the iodine cells. We appreciate the great assistance of the TROPOS lidar team during the field campaign.

Financial support

This work has been funded by the Bavarian Ministry of Economics and by the European Union within the EARLINET-ASOS project.

The article processing charges for this open-access publication are covered by the Karlsruhe Institute of Technology (KIT).

References

Alvarez II, R. A., Caldwell, L. M., Wolyn, P. G., Krueger, D. A., McKee T. B., and She, C. Y.: Profiling Temperature, Pressure, and Aerosol Properties Using a High Spectral Resolution Lidar Employing Atomic Blocking Filters, J. Atmos. Oceanic Tech., 10, 546-556, https://doi.org/10.1175/1520-0426(1993)010<0546:PTPAAP>2.0.CO;2, 1993.

Amodeo, A., Bösenberg, J., Ansmann, A., Balis, D., Böckmann, C., Chaikovsky, A., Comeron, A., Mitev, V., Papayannis, A., Pappalardo, G., Perrone, M. R., Rizi, V., Simeonov, V., Sobolewski, P., Spinelli, N., Stoyanov, D. V., Trickl, T., and Wiegner, M.: EARLINET: the European Aerosol Lidar Network, Optica Pura y Aplicada, 39, 1–10, 2006.

Ansmann, A., Riebesell, Maren, and Weitkamp, C.: Measurement of atmospheric aerosol extinction profiles with a Raman lidar, Opt. Lett., 15, 746-748, https://doi.org/10.1364/OL.15.000746, 1990.

Ansmann, A., Bösenberg, J., Chaikovsky, A. P., Comerón, A., Eixmann, R., Freudenthaler, V., Ginoux, P., Konguem, L., Linné, H., Márquez, M. Á. L., Manoj, S., Matthias, V., Mattis, I., Mitev, V., Müller, D., Nickovic, S., Pelon, J., Sauvage, L., Sobolewsky, P., Stohl, A., Torres, O., Vaughan, G., Wandinger, U. and Wiegner, M.: Long-range transport of Saharan dust to northern Europe: The 11-16 October 2001 outbreak with EARLINET. J. Geophys. Res., 108, 4783, doi: 10.1029/2003JD003757, 2003.

Ansmann, A., and Müller, D.: Lidar and Atmospheric Aerosol Particles, pp. 105-141 in: Lidar – Range-Resolved Optical Remote Sensing of the Atmosphere, Claus Weitkamp, Editor, Springer Series in Optical Sciences, ISSN 0342-4111, 455 pp., 2005.

https://doi.org/10.5194/egusphere-2026-5567
Preprint. Discussion started: 29 September 2026

Balis D, Amiridis, V., Nickovic, S., Papayannis, A., and Zerefos, C.: Optical properties of Saharan dust as detected by a Raman lidar at Thessaloniki, Greece, Geophys. Res. Lett., 31, L13104, doi: 10.1029/2004GL019881, 2004.

Bissonnette, L., Hutt, D., Hurtaud, Y., Stein, K., Weiß-Wrana, K., Trickl, T., Carnuth, W., Kunz, G., Moerman, M., Murphy, E. A., Turner, V., and Eaton, F. D.: Vertical Aerosol Structure Trial (VAST 1992), Defence Establishment Valcartier (Québec), 199 pp, 1995.

Bodermann B., Knöckel, H. and Tiemann, E.: Widely usable interpolation formulae for hyperfine splittings in the $^{127}I_2$ spectrum, Eur. Phys. D, 19, pp. 31-44, DOI: 10.1140/epjd/e20020052, 2002.

Böckmann, C., Wandinger, U., Ansmann, A., Bösenberg, J., Amiridis, V., Boselli, A., Delaval, A., De Tomasi, F., Frioud, M, Videnov Grigorov, I., Hågård, A., Horvat, M., Iarlori, M., Komguem, L., Kreipl, S., Larchevèque, G., Matthias, V., Papayannis, A., Pappalardo, G., Rocadenbosch, F., Rodrigues, J. A., Schneider, J., Shcherbakov, V., and Wiegner, M.: Aerosol lidar intercomparison in the framework of the EARLINET project. 2. Aerosol backscatter algorithm, Appl. Opt., 43, 977-989, https://doi.org/10.1364/AO.43.000977, 2004.

Bösenberg, J., Alpers, M., Althausen, D., Ansmann, A., Böckmann, C., Eixmann, R., Franke, A., Freudenthaler, V., Giehl, H., Jäger, H., Kreipl, S., Linné, H., Matthias, V., Mattis, I., Müller, D., Sarközi, J., Schneidenbach, L., Schneider, J., Trickl., T., Vorobieva, E., Wandinger U., and Wiegner, M.: The German Lidar Network: Methodology, Data, Analysis, Max-Planck-Institut für Meteorologie (Hamburg, Germany), Report No. 317, ISSN 0937-1060, Bösenberg, J., Alpers, M., Althausen, D., Ansmann, A., Böckmann, C., Eixmann, R., Franke, A., Freudenthaler, V., Giehl, H., Jäger, H., Kreipl, S., Linné, H., Matthias, V., Mattis, I., Müller, D., Sarközi, J., Schneidenbach, L., Schneider, J., Trickl., T., Vorobieva, E., Wandinger U., and Wiegner, M.: The German Lidar Network: Methodology, Data, Analysis, Max-Planck-Institut für Meteorologie (Hamburg, Germany), Report No. 317, ISSN 0937-1060, https://pure.mpg.de/rest/items/item_1560263_6/component/file_3033431/content, 155 pp., 2001.

Bristow, M. P., Bundy, D. H., and Wright, A. G.: Signal linearity, gain stability, and gating in photomultipliers: application to differential absorption lidars, Appl. Opt., 34, 4437-4452, https:// 10.1364/AO.34.004437, 1996.

Capelle, G. A., and Broida, H. P.: Lifetimes and quenching cross sections of I_2 (B $^2\Pi^+_{Ou}$), J. Chem. Phys., 58, 4212–4222, https://doi.org/10.1063/1.1678977, 1973.

Carswell, A. I., Houston, J. D., McNeil, W. R., Pal, S. R., and Sizgoric, S.: Remote probing by laser radar, Can. Aeronaut. Space J., 18, 335-336. 1972.

Carnuth W., and Reiter, R.: Cloud extinction profile measurements by lidar using Klett's inversion method, Appl. Opt., 25, 2899-2907, https://doi.org/10.1364/AO.25.002899, 1986.

Carnuth W., and Trickl, T.: Transport studies with the IFU three-wavelength aerosol lidar during the VOTALP Mesolcina experiment, Atmos. Environ., 34, pp. 1425-1434, https://doi.org/10.1016/S1352-2310(99)00423-9, 2000.

Carnuth, W., Kempfer, U., and Trickl, T.: Highlights of the tropospheric lidar studies at IFU within the TOR project, Tellus B, 54, 163-185, https://doi.org/10.3402/tellusb.v54i2.16656, 2002.

https://doi.org/10.5194/egusphere-2026-5567
Preprint. Discussion started: 29 September 2026

Damoah, R., Spichtinger, N., Servranckx, R., Fromm, M., Eloranta, E. W., Razenkov, I. A., James, P., Shulski, M., Forster, C., and Stohl, A.: A case study of pyro-convection using transport model and remote sensing data, Atmos. Chem. Phys., 6, 173–185, https://doi.org/10.5194/acp-6-173-2006, 2006.

De Boer, G., Eloranta, E. W., and Shupe, M. D.: Arctic Mixed-Phase Stratiform Cloud Properties from Multiple Years of Surface-Based Measurements at Two High-Latitude Locations, J. Atmos. Sci., 66, 2874-2887, https://doi.org/10.1175/2009JAS3029.1, 2009.

Draxler, R. and Hess, G.: An overview of the HYSPLIT_4 modelling system for trajectories, dispersion, and deposition, Aust. Meteorol. Mag., 47, 295–308, 1998.

Eloranta, E. E.: High Spectral Resolution Lidar, pp. 143-163 in: Lidar – Range-Resolved Optical Remote Sensing of the Atmosphere, Claus Weitkamp, Editor, Springer Series in Optical Sciences, ISSN 0342-4111, 455 pp., 2005.

Eloranta, E. W., and Razenkov, I. A.: Frequency locking to the center of a 532 nm iodine absorption line by using stimulated Brilouin scattering from a single-mode fiber, Opt. Lett., 31, 598-600, https://doi.org/10.1364/OL.31.000598, 2006.

Esselborn, M., Wirth, M., Fix, A., Tesche, M., and Ehret, G.: Airborne high spectral resolution lidar for measuring aerosol extinction and backscatter coefficients, Appl. Opt., 47, 346-358, https://doi.org/10.1364/AO.47.000346, 2008.

Fernald, F. G.: Analysis of atmospheric lidar observations: some comments, Appl. Opt., 23, 652–653, doi:10.1364/AO.23.000652, 1984.

Fiocco, G., Benedetti-Michelangeli, G., Maischberger, K., and Madonna, E.: Measurement of Temperature and Aerosol to Molecule Ratio, Nature Phys. Sci., 229, 78-79, https://doi.org/10.1038/physci229078a0, 1971.

Forkey, J. N.: Development and Demonstration of Filtered Rayleigh Scattering – A Laser Based Flow Diagnostic for Planar Measurement of Velocity, Temperature and Pressure, Dissertation, Princeton University, 297 pp. , 1996.

Freudenthaler, V.: Optimized background suppression in near field lidar telescopes, 6th ISTP International Symposium on Tropospheric Profiling: Needs and Technologies, Leipzig, Germany, 14. - 20. September 2003. DOI: 10.5282/ubm/epub.12957

Freudenthaler, V., Esselborn, M., Wiegner, M., Heese, B., Tesche, M., Ansmann, A., Müller, D., Althausen, D., Wirth, M., Fix, A., Ehret, G., Knippertz, P., Toledano, C., Gasteiger, J., Garhammer, M., and Seefeldner, M.: Depolarization ratio profiling at several wavelengths in pure Saharan dust during SAMUM 2006, Tellus B, 61, 165–179, doi:10.1111/j.1600-0889.2008.00396.x, 2009.

Freudenthaler, V.: The telecover test: A Quality assurance tool for the optical part of a lidar system, in: Reviewed and Revised Papers Presented at the 24th International Laser Radar Conference, Boulder, Colorado, USA, 23–27 June 2008, Vol. II, edited by: Hardesty, M. and Mayor, S., ISBN 978-0-615-21489-4, 145–146,2008.

Freudenthaler, V., Gross, S., Engelmann, R., Mattis, I., Wandinger, U., Pappalardo, G., Amodeo, A., Giunta, A., D'Amico, G., Chaikovsky, A., Osipenko, F., Slesar, A., Nicolae, D., Belegante, L., Talianu, C., Serikov, I., Linne, H., Jansen, F., Wilson, K., de Graaf, M., Apituley, A., Trickl, T., Giehl, H., and Adam, M.: EARLI09–

direct intercomparison of eleven EARLINET lidar systems, pp. 891–894 in: Proceedings of the 25th International Laser Radar Conference, St. Petersburg, Russia, 5–9 July, G. Matvienko, A. Zemlyanov, Eds., V. E. Zuev Institute of Optics (Tomsk, Russia), 2010.

Freudenthaler, V., Linné, H., Chaikovski, A., Rabus, D., and Groß, S.: EARLINET lidar quality assurance tools, Atmos. Meas. Tech. Discuss., https://doi.org/10.5194/amt-2017-395, 35 pp., 2018.

Forster, C., Wandinger, U., Wotawa, G., James, P., Mattis, I., Althausen, D., Simmonds, P., O'Doherty, S., Jennings, S. G., Kleefeld, C., Schneider, J., Trickl, T., Kreipl, S., Jäger, H., and Stohl, A.: Transport of boreal forest fire emissions from Canada to Europe, J. Geophys. Res., 106, 22887-22906, https://doi.org/10.1029/2001JD900115, 2001.

Giehl, H., and Trickl, T.: Testing the IFU High-Spectral-Resolution Lidar at the 2009 Leipzig Field Campaign, pp. 920-923 in: Proceedings of the 25th International Laser Radar Conference, St.-Petersburg (Russia), July 5 to 9, 2010, G. Matvienko, A. Zemlyanov, Eds., V. E. Zuev Institute of Optics (Tomsk, Russia), 2010.

Groß, S., Freudenthaler, V., Schepanski, K., Toledano, C., Schäfler, A., Ansmann, A., and Weinzierl, B.: Optical properties of long-range transported Saharan dust over Barbados as measured by dual-wavelength depolarization Raman lidar measurements, Atmos. Chem. Phys., 15, 11067–11080, https://doi.org/10.5194/acp-15-11067-2015, 2015.

Grund, C. J., and Eloranta, E. W.: University of Wisconsin High Spectral Resolution Lidar, Opt. Engin., 30, 6-12, https://doi.org/10.1117/12.55766, 1991.

Gutkowicz-Krusin, D.: Multiangle lidar performance in the presence of horizontal inhomogeneities in atmospheric extinction and scattering, Appl. Opt., 32, 3266–3272, https://doi.org/10.1364/AO.32.003266, 1993.

Hair, J. W., Caldwell, L. M., Krueger, D. A., and She, C.-Y.: High-spectral-resolution lidar with iodine-vapor filters: measurement of atmospheric-state and aerosol profiles, Appl. Opt., 40, 5280-5294, https://doi.org/10.1364/AO.40.005280, 2001.

Hair, J. W., Hostetler, C. A., Cook, A. L., Harper, D. B., Ferrare, R. A., Mack, T. L., Welsh, W., Izquierdo, L. R., and Hovis, F. E.: Airborne high spectral resolution lidar for profiling aerosol optical properties, Appl. Opt., 47, 6734-6752, https://doi.org/10.1364/AO.47.006734, 2008.

Hartung, J., Seedorf, J. Trickl, T. and Gronauer, H.: Freisetzung partikelförmiger Stoffe aus einem Schweinestall mit zentraler Abluftführung in die Stallumgebung, Dtsch. tierärztl. Wschr., 105, pp. 244-245, ISSN: 0341-6593, 1998.

Hayman, M., and Spuler, S.: Demonstration of a diode-laser-based high-spectral-resolution lidar (HSRL) for quantitative profiling of cloud and aerosols, Opt. Exp., A1096-A1110, https://doi.org/10.1364/OE.25.0A1096, 2017.

Iarlori, M., Madonna, F., Rizi, V., Trickl, T., and Amodeo, A.: Effective resolution concepts for lidar observations, Atmos. Meas. Tech., 8, 5157–5176, https://doi.org/10.5194/amt-8-5157-2015, 2015.

Jäger, H.: Long-term record of lidar observations of the stratospheric aerosol layer at Garmisch-Partenkirchen, *J.* Geophys. Res., 110, D08106, doi: 10.1029/ 2004JD005506, 9 pp., 2005.

Jäger, H., Carnuth, W. and Georgii, B.: Observations of Saharan dust at a North Alpine mountain station. J. Aerosol Sci., 19, 1235–1238, 1988.

https://doi.org/10.5194/egusphere-2026-5567
Preprint. Discussion started: 29 September 2026

Klett, J. D.: Stable analytical inversion solution for processing lidar returns, Appl. Opt., 20, 211-220, https://doi.org/10.1364/AO.20.000211, 1981.

Klett, J. D.: Lidar inversion with variable backscatter/extinction ratios, Appl. Opt., 24, 1638-1643, https://doi.org/10.1364/AO.24.001638, 1985.

Knöckel H., Bodermann, B., and Tiemann, E.: High precision description of the rovibronic structure of the I_2 B–X spectrum, Eur. Phys. D, 28, pp. 199-209, DOI: 10.1140/epjd/e2003-00313-4, 2004.

Koschmieder, H.: Theorie der horizontalen Sichtweite, Beiträge zur Physik der Atmosphäre, XII, 33-53, 1925a (in German).

Koschmieder, H.: Theorie der horizontalen Sichtweite, II.. Kontrast und Sichtweite, Beiträge zur Physik der Atmosphäre, XII, 171-181, 1925b (in German).

Kreipl, S.: Messung des Aerosoltransports am Alpennordrand mittels Laserradar (Lidar), Dissertation, Friedrich-Alexander-Universität Erlangen-Nürnberg (Germany), 195 pp., 2006 (in German)

Kunz, G. J, and de Leuw, G.: Inversion of lidar signals with the slope method, Appl. Opt, 32, 3248-3256, doi: 10.1364/AO.32.003249, 1993.

Kunz G. J., and Trickl, T., Lidar Measurements of Atmospheric Extinction during the MAPTIP Trial, Proc. SPIE, 2828, 31-38, https://publications.tno.nl/publication/34620735/PalXwx/kunz-1996-lidar.pdf, 1996.

Leblanc, T., Sica, R. J., van Gijsel, J. A. E., Godin-Beekmann, S., Haefele, A., Trickl, T., Payen, G., and Gabarrot, F.: Proposed standardized definitions for vertical resolution and uncertainty in the NDACC lidar ozone and temperature algorithms – Part 1: Vertical resolution, Atmos. Meas. Tech., 9, 4029–4049, https://doi.org/10.5194/amt-9-4029-2016, 2016.

Liu, Z., Matsui, I., and Sugimoto, N.: High-spectral-resolution lidar using an iodine absorption filter for atmospheric measurements, Opt. Eng., 38, 1661-1670, https://doi.org/10.1117/1.602218, 1999.

Mamouri, R. E., Ansmann, A., Nisantzi, A., Kokkalis, P., Schwarz, A., and Hadjimitsis, D.: Low Arabian dust extinction-to-backscatter ratio, Geophys. Res. Lett., 40, 4762–4766, doi:10.1002/grl.50898, 2013.

Müller, D., Mattis, I., Wandinger, U., Ansmann, A., Althausen, D., Dubovik, O., Eckhardt, S. and Stohl, A.: Saharan dust over a Central European EARLINET-AERONET site: Combined observations with Raman lidar and Sun photometer, J. Geophys. Res., 108, 4345, doi: 10.1029/2002JD002918, 2003.

Müller, D., Ansmann, A., Mattis, I., Tesche, M., Wandinger, U., Althausen, D., and Pisani, G.: Aerosol-type-dependent lidar ratios observed with Raman lidar, J. Geophys. Res., 112, D16202, doi:10.1029/2006JD008292, 2007.

Nisantzi, A., Mamouri, R. E., Ansmann, A., Schuster, G. L., and Hadjimitsis, D. G.: Middle East versus Saharan dust extinction-to-backscatter ratios, Atmos. Chem. Phys., 15, 7071–7084, https://doi.org/10.5194/acp-15-7071-2015, 2015.

Owens, J. C.: Optical refractive index of air: dependence on pressure, temperature and composition, Appl. Opt., 6, 51-59, https://doi.org/10.1364/AO.6.000051, 1967.

Papanikolaou, C.-A., Papayannis, A., Gidarakou, M., Abdullaev, S. F., Ajtai, N., Baars, H., Balis, D., Bortoli, D., Bravo-Aranda, J. A., Collaud-Coen, M., de Rosa, B., Dionisi, D., Eleftheratos, K., Engelmann, R., Floutsi,

https://doi.org/10.5194/egusphere-2026-5567
Preprint. Discussion started: 29 September 2026

A. A., Abril-Gago, J., Goloub, P., Giuliano, G., Gumà-Claramunt, P., Hofer, J., Hu, Q., Komppula, M., Marinou, E., Martucci, G., Mattis, I., Michailidis, K., Muñoz-Porcar,, C., Mylonaki, M., Mytilinaios, M., Nicolae, D., Rodríguez-Gómez, A., Salgueiro, V., Shang, X., Stachlewska, I. S., □tefănie, H. I., Szczepanik, D., Trickl, T., Vogelmann, H., and Voudouri, K. A.: Observations of an Unprecedented Saharan Dust Event Across the European Continent During Spring 2022, Remote Sens., 16,, 3350, 28 pp., https://doi.org/10.3390/rs16173350, 2024.

Pappalardo, G., Amodeo, A., Apituley, A., Comeron, A., Freudenthaler, V., Linné, H., Ansmann, A., Bösenberg, J., D'Amico, G., Mattis, I., Mona, L., Wandinger, U., Amiridis, V., Alados-Arboledas, L., Nicolae, D., and Wiegner, M.: EARLINET: towards an advanced sustainable European aerosol lidar network, Atmos. Meas. Tech., 7, 2389–2409, https://doi.org/10.5194/amt-7-2389-2014, 2014.

Piironen, P., and Eloranta, E. W.: Demonstration of a high-spectral-resolution lidar based on an iodine absorption filter, Opt. Lett., 19, 234-236, https://doi.org/10.1364/OL.19.000234, 1994.

Reid, J. S., Kuehn, R. E., Holz, R. E., Eloranta, E. W., Kaku, K. C., Kuang, S., Newchurch, M. J., Thompson, A. M., Trepte, C. R., Zhang, J., Atwood, S. A., Hand, J. L., Holben, B. N., Minnis, P., and Posselt, D. J.: Ground-based High Spectral Resolution Lidar observation of aerosol vertical distribution in the summertime Southeast United States, , J. Geophys. Res., 122, 2970–3004, doi:10.1002/ 2016JD025798, 2017.

Pappalardo, G.: Lidar ratio data base, pp. 148–151 in: EARLINET: a European Aerosol Research Lidar Network to Establish an Aerosol Climatology, Final Report, European Union, J. Bösenberg and V. Matthias, Eds. published as Max-Planck-Institut für Meteorologie, Report No. 348 (Hamburg, Germany), ISSN 09371060, 2003.

Pappalardo, G., Amodeo, A., Apituley, A., Comeron, A., Freudenthaler, V., Linné, H., Ansmann, A., Bösenberg, J., D'Amico, G., Mattis, I., Mona, L., Wandinger, U., Amiridis, V., Alados-Arboledas, L., Nicolae, D., and Wiegner, M.: EARLINET: towards an advanced sustainable European aerosol lidar network, Atmos. Meas. Tech., 7, 2389–2409, doi:10.5194/amt-7-2389-2014, 2014.

Papayannis A., Amiridis, V., Mona, L., Tsaknakis, G., Balis, D., Bösenberg, J., Chaikovsky, A., De Tomasi, F., Grigorov, I., Mattis, I., Mitev, V., Müller, D., Nickovic, S., Pérez, C., Pietruczuk, A., Pisani, G. L., Ravetta, F., Rizi, V., Sicard, M., Trickl, T., Wiegner, M., Gerding, M., Mamouri, R. E., D´Amico, G., and Pappalardo, G.: Systematic lidar observations of Saharan dust over Europe in the frame of EARLINET (2000-2002), J. Geophys. Res., 113, D10204, doi: 10.1029/2007JD009028, 17 pp., 2008.

Reiter, R., Littfaß, M., Carnuth, W., and Funk, W.: Lidar Measurements of Concentrations and Size Distribution Profiles of Tropospheric Aerosol", pp. 82-84 in: 9th International Laser Radar Conference, C. Werner, F. Köpp, Eds., DFVLR (Oberpfaffenhofen, Germany), 1979.

Reiter R., Carnuth, W. and Sladkovic, R.: Behavior of Tropospheric Aerosol Profiles Monitored by Lidar, Compared with Independently Recorded Data of Aerosol Structure and Aerological Profiles, pp. 109 -112 in: 12th International Laser Radar Conference, G. Mégie, Ed., CNRS (Paris, France), 1984.

Sasano, Y., and Nakane, H.: Quantitative Analysis of RHI Lidar by an Iterative Adjustment of the Boundary Condition Term in the Lidar Solution, Appl. Opt., 26, 615–616, https://doi.org/10.1364/AO.26.000615, 1987.

https://doi.org/10.5194/egusphere-2026-5567
Preprint. Discussion started: 29 September 2026

Schweitzer, W. G., Kessler, E. G., Deslattes, R. D., Layer, H. P., and Whetstone, J. R.: Description, Performance, and Wavelengths of Iodine Stabilized Lasers, Appl. Opt., 12, 2927-2938, https://doi.org/10.1364/AO.12.002927, 1973.

She, C. Y.: Spectral structure of laser light scattering revisited: bandwidths of nonresonant scattering lidars, Appl. Opt., 40, 4875-4884, https://doi.org/10.1364/AO.40.004875, 2001.

Shen, F., Xie, C., Qiu, C., and Wang, B.: Fabry-Perot etalon-based ultraviolet trifrequency high-spectral-resolution lidar for wind , temperature, and aerosol measurements from 0.2 to 35 km altitude, Appl. Opt., 31, 9328-9340, https://doi.org/10.1364/AO.57.009328, 2018.

Shimizu, H., Lee, S. A., and She, C. Y.: High spectral resolution lidar system with atomic blocking filters for measuring atmospheric parameters, Appl. Opt., 22, 1373-1380, https://doi.org/10.1364/AO.22.001373, 1983.

Shipley, S. T., Tracy, D. H., Eloranta, E. W., Trauger, J. T., Sroga, J. T., Roesler, F. L., and Weinman, J. A.: High spectral resolution lidar to measure optical scattering properties of atmospheric aerosols, 1: Theory and instrumentation, Appl. Opt., 22, 3716-3724, https://doi.org/10.1364/AO.22.003716, 1983.

Speidel, J., and Vogelmann, H.: Correct(ed) Klett–Fernald algorithm for elastic aerosol backscatter retrievals: a sensitivity analysis, Appl. Opt., 62, 861-868, https://doi.org/10.1364/AO.465944, 2023.

Spinhirne, J. D., Reagan, J. A., and Herman, B. M.: Vertical Distribution of Aerosol Extinction Cross Section and Inference of Aerosol Imaginary Index in the Troposphere by Lidar Technique, J. Appl. Meteorol. 19, 426–438, https://doi.org/10.1175/1520-0450(1980)019<0426:VDOAEC>2.0.CO;2, 1980.

Sroga, J. T., Eloranta, E. W., Shipley, S. T., Roesler, F. L., and Tyron, P. J.: High spectral resolution lidar to measure optical scattering properties of atmospheric aerosols, 2: Calibration and data analysis, Appl. Opt., 22, 3725-3732, https://doi.org/10.1364/AO.22.003725, 1983.

Stein, A. F., Draxler, R. R, Rolph, G. D., Stunder, B. J. B., Cohen, M. D., and Ngan, F.: NOAA's HYSPLIT atmospheric transport and dispersion modeling system, Bull. Am. Meteorol. Soc., 96, 2059–2077, https://doi.org/10.1175/BAMS-D-14-00110.1, 2015.

Tenti, G., Boley, C. D., and Desai, R. C.: On the kinetic model description of Rayleigh-Brillouin scattering from molecular gases, Can. J. Phys., 52, 285-290, https://doi.org/10.1139/p74-041, 1974.

Trickl, T.: Upgraded 1.56-µm lidar at IMK-IFU with 0.28 J/pulse, Appl. Opt., 49, 3732-3740, https://doi.org/10.1364/AO.49.003732, 2010.

Trickl T., Kung, A. H., and Lee, Y. T.: Krypton atom and testing the limits of extreme-ultraviolet tunable-laser spectroscopy, Phys. Rev. A, 75, 022501, 13 pp., DOI: https://doi.org/10.1103/PhysRevA.75.022501, 2007.

Trickl, T., Neidl, F., Giehl, H., Perfahl, M., and Vogelmann, H.: Three decades of tropospheric ozone lidar development at Garmisch-Partenkirchen, Atmos. Meas. Tech., 13, 6357-6390, https://doi.org/10.5194/amt-13-6357-2020, 2020.

Trickl, T., Vogelmann, H., Fromm, M. D., Jäger, H., Perfahl, M., and Steinbrecht, W.: Measurement report: Violent biomass burning and volcanic eruptions – a new period of elevated stratospheric aerosol over central Europe (2017 to 2023) in a long series of observations, Atmos. Chem. Phys., 24, 1997–2021, https://doi.org/10.5194/acp-24-1997-2024, 2024.

https://doi.org/10.5194/egusphere-2026-5567
Preprint. Discussion started: 29 September 2026

Trickl, T., Vogelmann, H., Bittner, M., Nedoluha, G., Schmidt, C., Steinbrecht, W., and Wüst, S.: Temperature profiles combined from lidar and airglow measurements, Atmos. Meas. Tech., 18, 7477-7496, https://doi.org/10.5194/amt-18-7477-2025, 2025.

Velchev, I., van Dierendonk, R., Hogervorst, W., and Ubachs, W.: A Dense Grid of Reference Iodine Lines for Optical Frequency Calibration in the Range 571–596 nm, J. Mol. Spectrosc., 187, 21-27, doi: 10.1006/jmsp.1997.7480, 1998.

Vogelmann, H. and Trickl, T.: Wide-Range Sounding of Free-Tropospheric Water Vapor with a Differential-Absorption Lidar (DIAL) at a High-Altitude Station, Appl. Opt., 47, 2116-2132, https://doi.org/10.1364/AO.47.002116, 2008.

Wandinger, U., Freudenthaler, V., Baars, H., Amodeo, A., Engelmann, R., Mattis, I., Groß, S., Pappalardo, G., Giunta, A., D'Amico, G., Chaikovsky, A., Ossipenko, F., Slesar, A., Nicolae, D., Belegante, L., Talianu, C., Serikov, I., Linné, H., Jansen, F., Apituley, A., Wilson, K., de Graaf, M., Trickl, T., Giehl, H., Adam, M., Comeron, A., Muñoz-Porcar, C., Rocadenbosch, F., Sicard, M., Tomás, S., Lange, D., Kumar, D., Pujadas, M., Molero, F., Fernandez, A. J., Alados Arboledas, L., Bravo-Aranda, J. A., Navas-Guzmán, F., Guerrero-Rascado, J, L., Granados-Munoz, M. J.. Preißler, J., Wagner, F., Gausa, M., Grigorov, I., Stoyanov, D., Iarlori, M., Rizi, V., Spinelli, N., Boselli, A., Wang, X., Lo Feudo, T., Perrone, M. R., De Tomasi, F., and Burlizzi, P.: EARLINET instrument intercomparison campaigns: Overview on strategy and results, Atmos. Meas. Tech., 9, 1001-1023, https://doi.org/10.5194/amt-9-1001-2016, 2016.

U.S. Standard Atmosphere: National Oceanic and Atmospheric Organization (NOAA), National Aeronautics and Space Administration, United States Air Force, NOAA-S/T 76-1562, US Printing Office (Washington, D.C.), 227 pp., 1976.

VDI: Fernmeßverfahren, Messungen in der Atmosphäre nach dem LIDAR-Prinzip, Messen gasförmiger Luftverunreinigungen mit dem DAS-LIDAR / Remote sensing, atmospheric measurements with LIDAR, Measuring gaseous air pollution with DAS LIDAR, Guideline VDI 4210, Part 1, Verein Deutscher Ingenieure (Düsseldorf, Germany), 47 pp., 1999.

Volkamer, R., Baidar, S., Campos, T. L., Coburn, S., DiGangi, J. P., Dix, B., Eloranta, E. W., Koenig, T. K., Morley, B., Ortega, I,. Pierce, B. R., Reeves, M., Sinreich, R., Wang, S., Zondlo, M. A., and Romashkin, P. A.: Aircraft measurements of BrO, IO, glyoxal, NO_2, H_2O, O_2–O_2 and aerosol extinction profiles in the tropics: comparison with aircraft-/ship-based in situ and lidar measurements, Atmos. Meas. Tech., 8, 2121–2148, https://doi.org/10.5194/amt-8-2121-2015, 2015.

Wandinger, U., Raman Lidar, pp. 241-271 in: Lidar – Range-Resolved Optical Remote Sensing of the Atmosphere, Claus Weitkamp, Editor, Springer Series in Optical Sciences, ISSN 0342-4111, 455 pp., 2005.

Witschas, B.: Analytical model for Rayleigh-Brillouin line shapes in air, Appl. Opt., 50, 267–270, https://doi.org/10.1364/AO.50.000267, 2011a.

Witschas, B.: Analytical model for Rayleigh-Brillouin line shapes in air, erratum, Appl. Opt., 50, p. 5758, https://opg.optica.org/ao/abstract.cfm?uri=ao-50-29-5758, 2011b.

WMO: Atmospheric Ozone 1985 Assessment of our Understanding of the Processes Controlling its Present Distribution and Change, Report No. 16, Vol. I, World Meteorological Organization, Geneva (Switzerland), 264 pp., 1986.

https://doi.org/10.5194/egusphere-2026-5567
Preprint. Discussion started: 29 September 2026

Xu, S. C., van Dierendonk, R., Hogervorst, W., and Ubachs, W.: A Dense Grid of Reference Iodine Lines for Optical Frequency Calibration in the Range 595–655 nm, J. Mol. Spectrosc., 201, 256-266, doi: 10.1006/jmsp.2000.8085, 2000.

https://doi.org/10.5194/egusphere-2026-5567
Preprint. Discussion started: 29 September 2026

Figures:

Fig. 1. Three-wavelength mobile aerosol lidar of IMK-IFU on the parking area of TROPOS in Leipzig; in the background the EARLINET lidar from Bucharest is seen, to the left the shadow of the MULIS system from Munich. The cover of the lidar compartment is shifted backward. The lidar box (white and orange) can be rotated in azimuth and elevation. The elevation angle is measured with the goniometer to the left. For the lidar measurements an elevation angle of 85 degrees was chosen as demanded by the organizers. The two flaps to the left are opened for the air circulation of the water-cooling unit of the laser power supply.

https://doi.org/10.5194/egusphere-2026-5567
Preprint. Discussion started: 29 September 2026

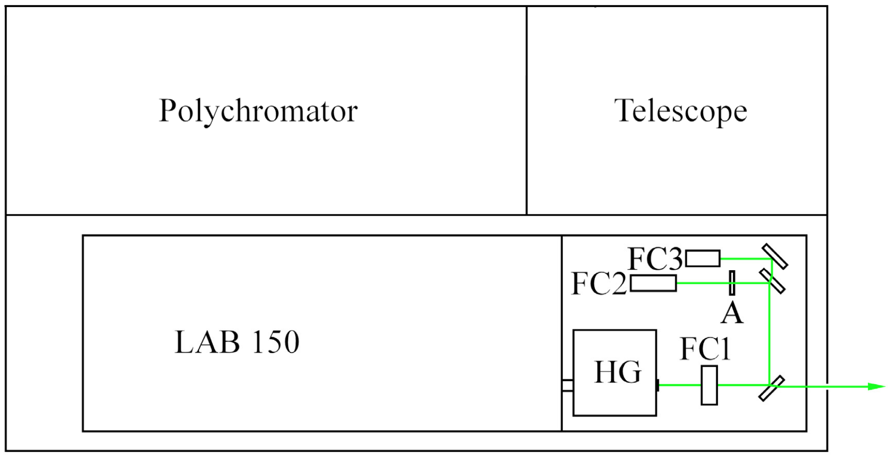

Fig. 2. Assembly drawing of the orange-white lidar box in Fig. 1 (top view): HG ..... harmonic generator (output: 1064.4 nm, 532.2 nm, 354.8 nm), FC1 ..... fibre coupler 1 (for energy measurements), FC2 ..... fibre coupler 2 (for the single-mode fibre to the wave meter), FC3 ..... fibre coupler 3 (for trigger), A ..... attenuator (neutral-density filter from Andover); the laser compartment is cooled by air from an external refrigerator to maintain a stable temperature. The cover of the polychromator contains an interlock switching off the detector power supply if opened. The two beam splitters are optimized to reflect a small amount of the 532-nm component and to transmit completely the radiation at 1064 and 355 nm (necessary to avoid damaging the single-mode fibre of the wavemeter).

https://doi.org/10.5194/egusphere-2026-5567
Preprint. Discussion started: 29 September 2026

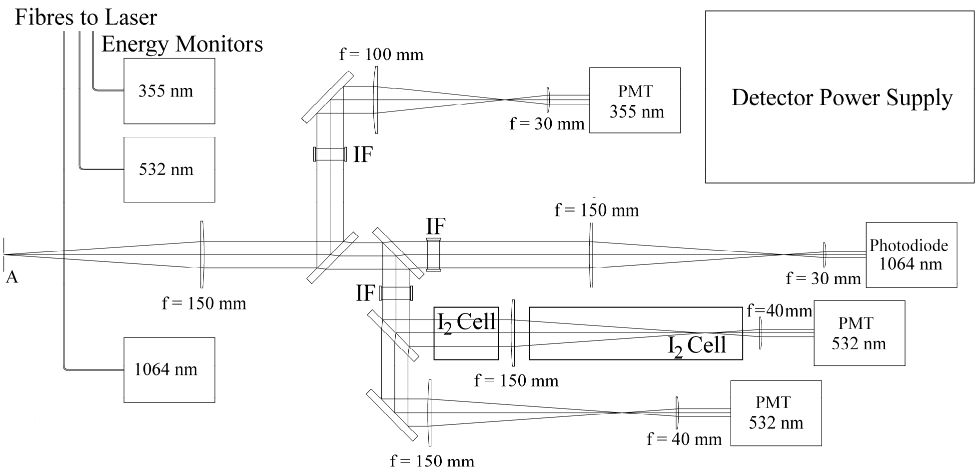

Fig. 3. Layout of the lidar receiver; the energy monitors for the lidar calibration are not yet used. The abbreviation IF means interference filter, A is an adjustable-slit aperture in the focal plane of the telescope. The lidar detectors (three PMTs and one PIN diode) are drawn at the right-hand side labelled with the corresponding radiation wavelength. Three pin diodes (left) were installed for monitoring the respective laser pulse energies.

https://doi.org/10.5194/egusphere-2026-5567
Preprint. Discussion started: 29 September 2026

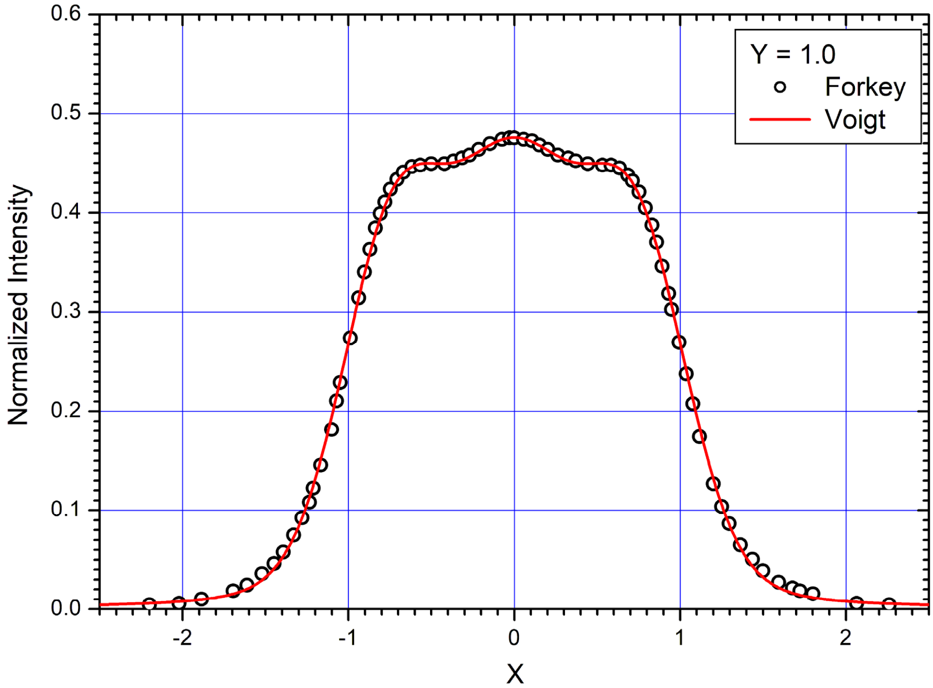

Fig. 4. Approximation of the Y = 1 Rayleigh-Brillouin spectrum with three Voigt lines; The expression "Normalized intensity" is adopted from Forkey (1996).

https://doi.org/10.5194/egusphere-2026-5567
Preprint. Discussion started: 29 September 2026

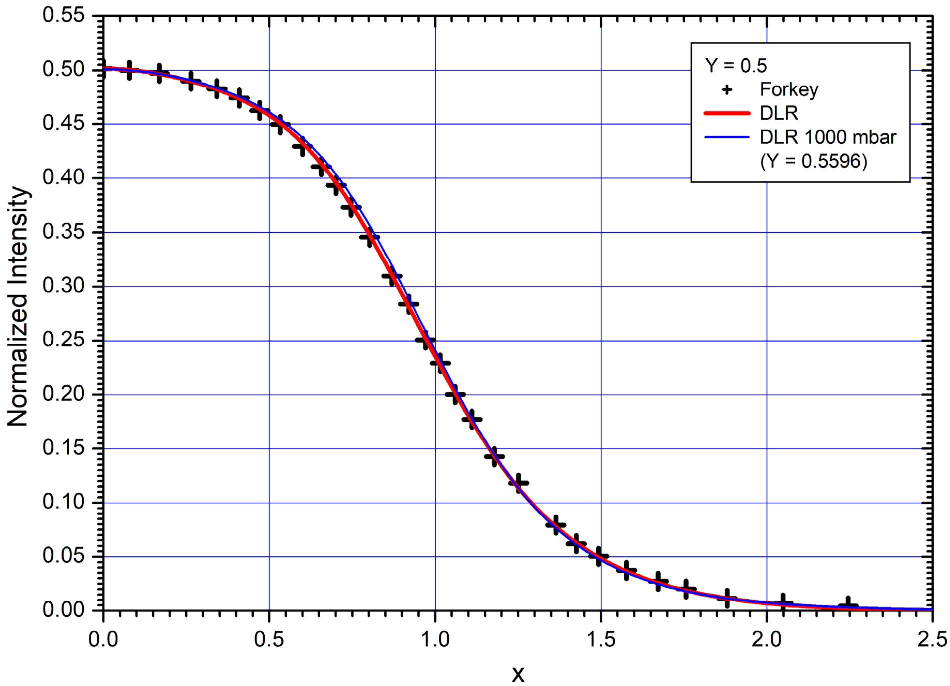

Fig. 5. Comparison of calculations with the Witschas (2011) algorithm (DLR) with line data from (Forkey, 1996) for Y = 0.5 and a calculation for Y = 0.5596 (300 K, 1000 mbar)

https://doi.org/10.5194/egusphere-2026-5567
Preprint. Discussion started: 29 September 2026

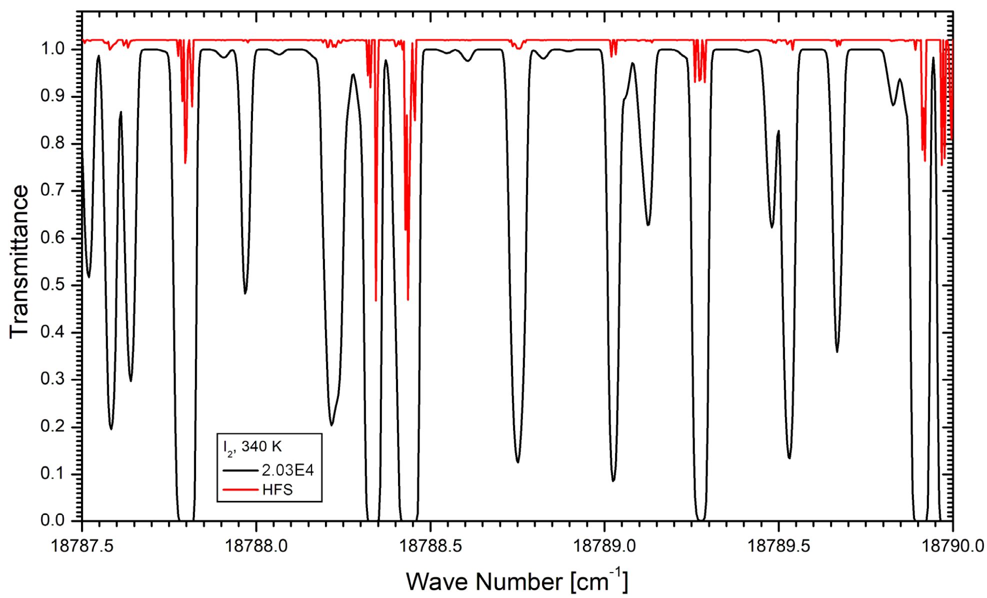

Fig. 6. Calculated iodine absorption spectra for 340 K: the raw spectrum is multiplied by 20300 (black) which sets the line minimum at 18789.2770 cm^{-1} to 8×10^{-4} when applying the Beer-Lambert law. The partly resolved hyperfine spectrum (HFS) is given in red.

https://doi.org/10.5194/egusphere-2026-5567
Preprint. Discussion started: 29 September 2026

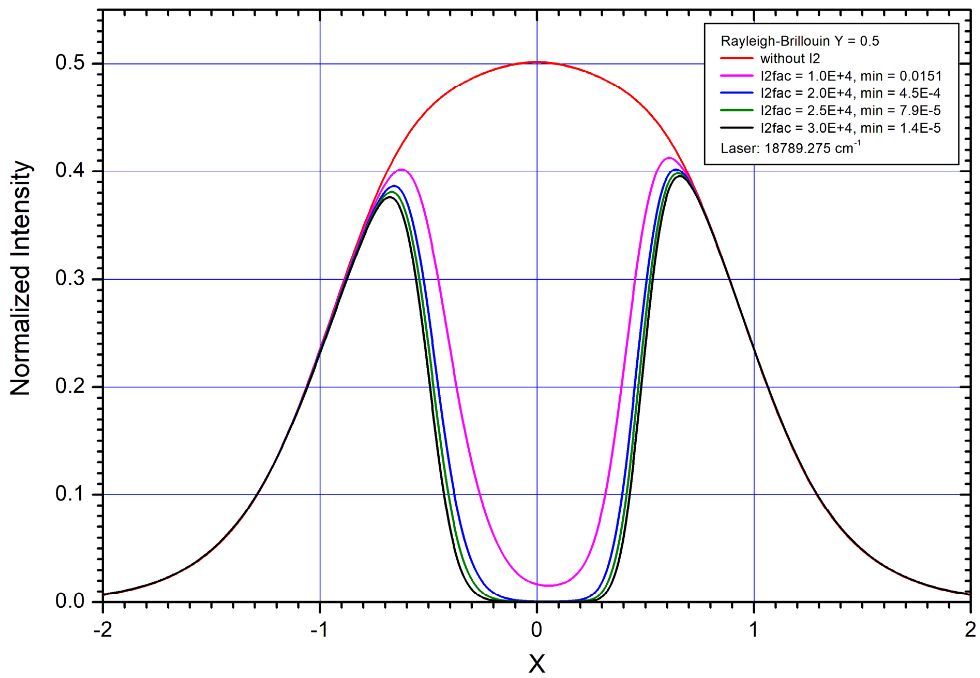

Fig. 7. Calculated line shapes around 18789.2770 cm^{-1} based on the approximated Y = 0.5 Tenti curve (Forkey, 1996) and four different iodine scaling factors (I2fac); X = 1 corresponds to 1.558 GHz (for 300 K). The minimum signals (min) are given in the legend.

https://doi.org/10.5194/egusphere-2026-5567
Preprint. Discussion started: 29 September 2026

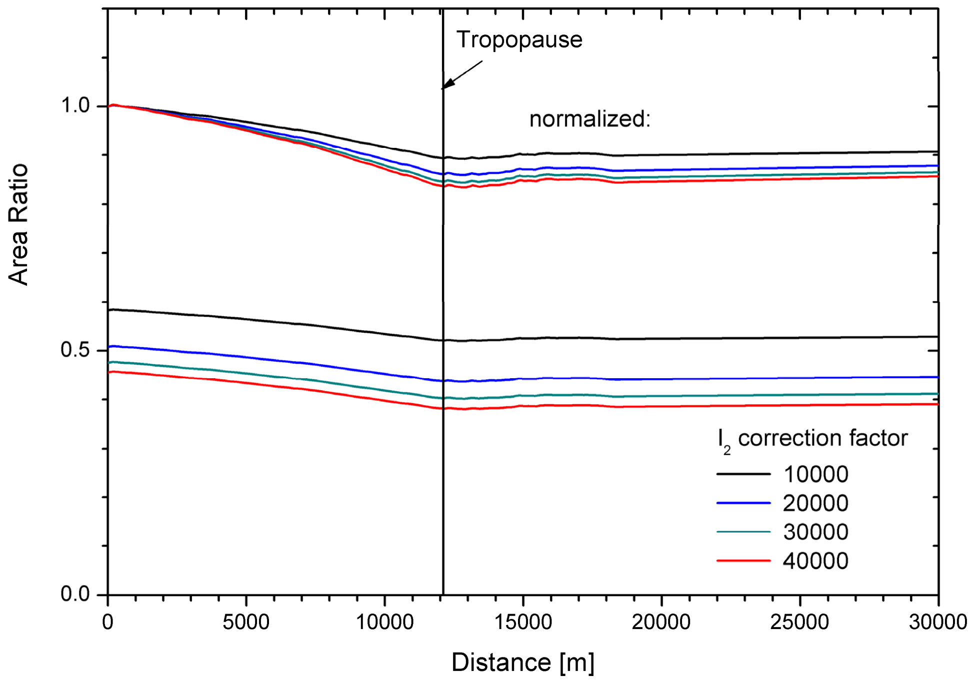

Fig. 8. Area ratios of iodine-depleted line and full backscattered spectral line (red curve in Fig. 7) for four different multiplication (correction) factors for the IodineSpec4 output. As seen in Fig. 7 the area ratio decreases with growing I_2 correction factor. The atmospheric density is obtained from a radiosonde ascent at Leipzig on 25 May 2009 launched at 21:15 CET. Since just the slope of the area ratio matters in the retrieval also the curves are given normalize to 1.0 at distance r = 0 and reveal just minor differences for I_2 correction factors ≥ 20000. The tropopause presented here is the thermal value defined by the World Meteorological Organisation (WMO, 1986).

https://doi.org/10.5194/egusphere-2026-5567
Preprint. Discussion started: 29 September 2026

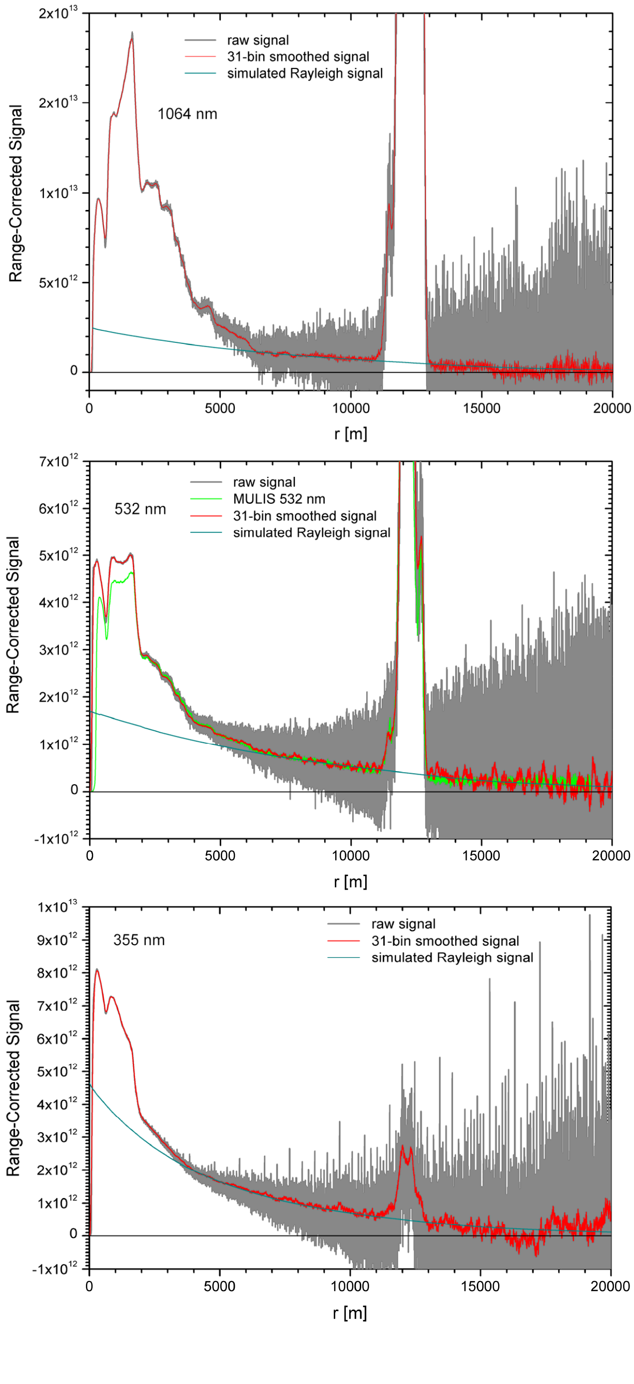

Fig. 9. Corrected backscatter profiles of channels 1 (354.8 nm, bottom), 2 (532.2 nm, middle) and 4 (1064.4 nm, top) of the IFU HSRL on 25 May, 2009, accumulated between 22:00 and 22:59 CET: The noisy grey curves represent the raw data, the red curves ±15 bin sliding arithmetic averages. In the 532.2-nm panel also the MULIS backscatter profile is given for comparison, calibrated to match that of channel 2 above 3 km. For comparison, simulated Rayleigh backscatter profiles are shown, calibrated above 6.3 km.

https://doi.org/10.5194/egusphere-2026-5567
Preprint. Discussion started: 29 September 2026

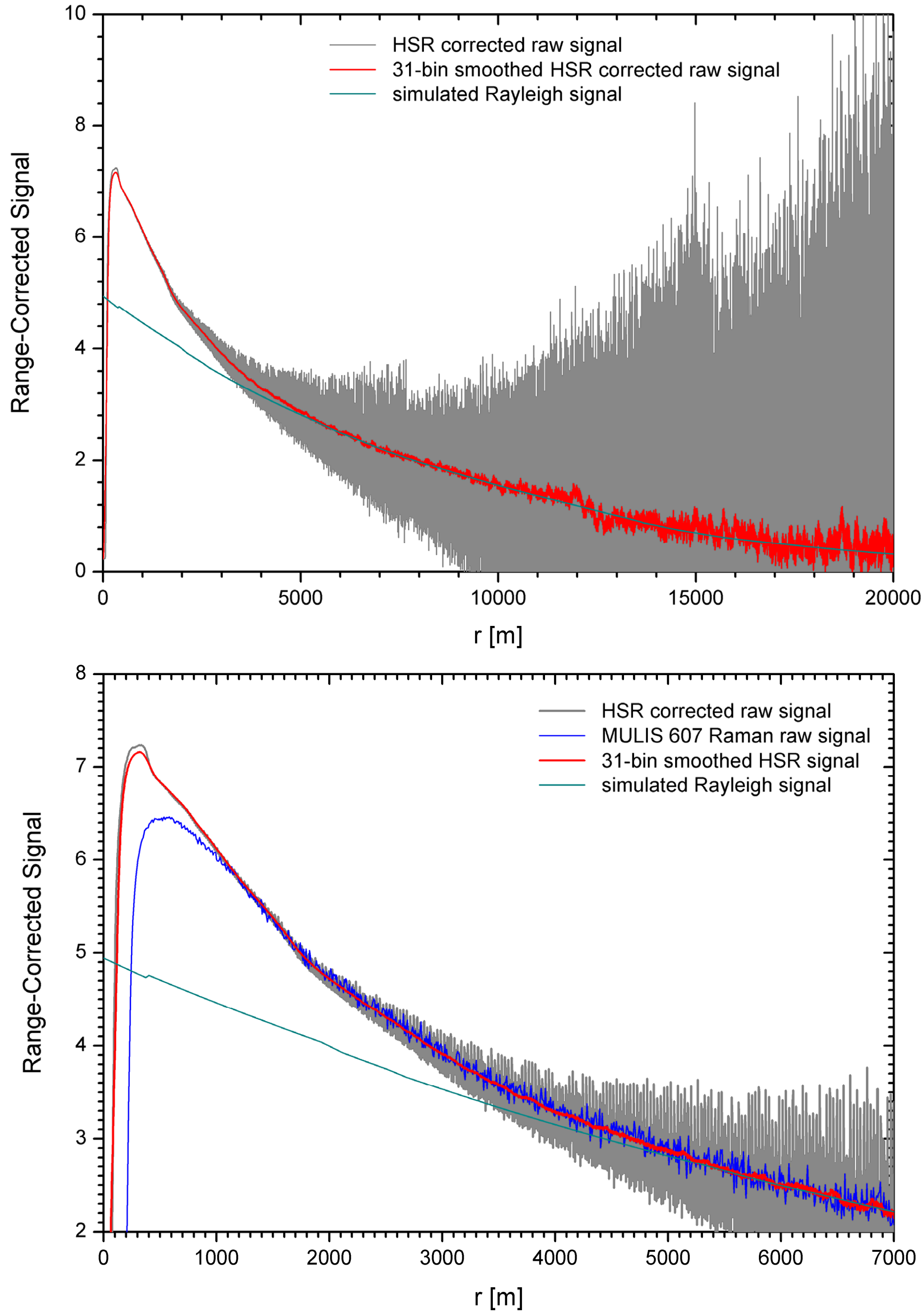

Fig. 10. Corrected 532.2-nm HSR aerosol backscatter signal accumulated on 25 May, 2009, between 22:00 and 22:59 CET (grey) together with ±15 bin sliding arithmetic averages (red) and (lower panel) the MULIS 607-nm Raman backscatter profile (blue) from photon counting; in the upper panel the strong downward slope between 11.8 and 12.7 km is caused by the cirrus. Above 10 km residual ripple becomes visible.

https://doi.org/10.5194/egusphere-2026-5567
Preprint. Discussion started: 29 September 2026

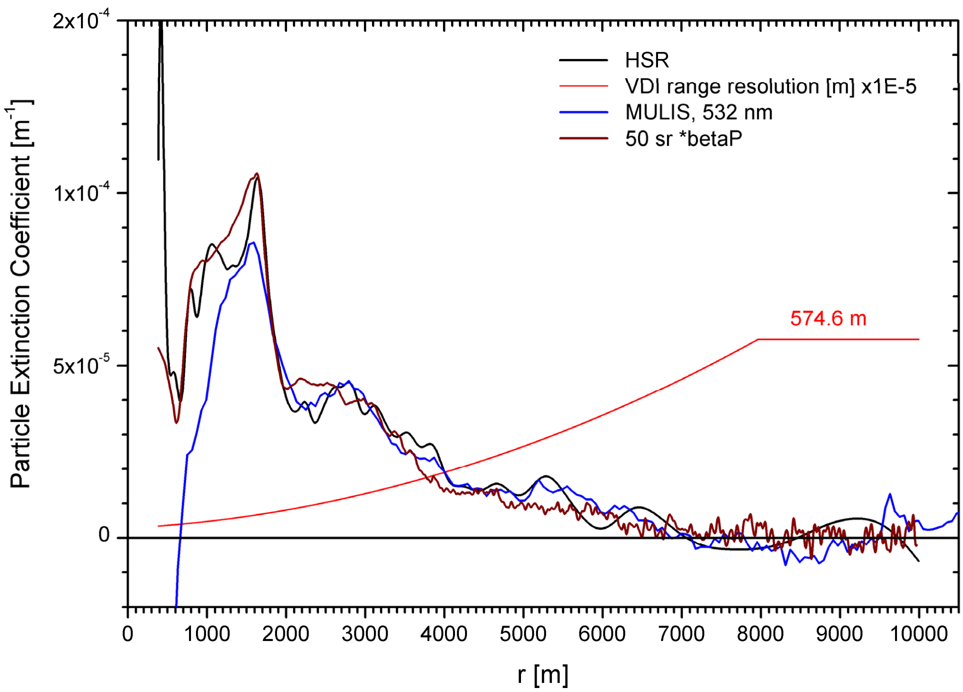

Fig. 11. 532.2-nm extinction coefficients from the HSR channel (channel 3, black) and the MULIS Raman channel (from Wandinger et al., 2016, blue). For comparison, β_P×(50 sr) from inserting the α_P from the HSR retrieval into the lidar equation for the unfiltered channel (channel 2) is also shown (wine red).

https://doi.org/10.5194/egusphere-2026-5567
Preprint. Discussion started: 29 September 2026

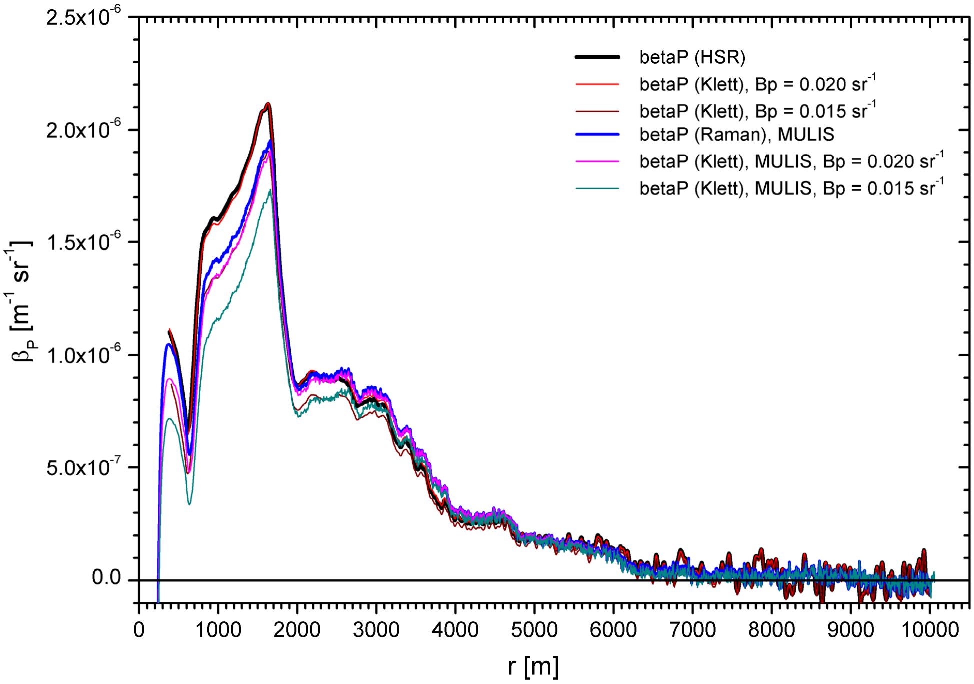

Fig. 12. 532.2-nm particle backscatter coefficients from the HSR and Klett (channel 2) solutions compared with the corresponding MULIS profiles. The Klett inversions were calculated for the backscatter-to-extinction ratios $B_P = 0.020$ sr^{-1} and $B_P = 0.015$ sr^{-1}. Below 2 km, the wine red and magenta curves are difficult to separate visually.

https://doi.org/10.5194/egusphere-2026-5567
Preprint. Discussion started: 29 September 2026

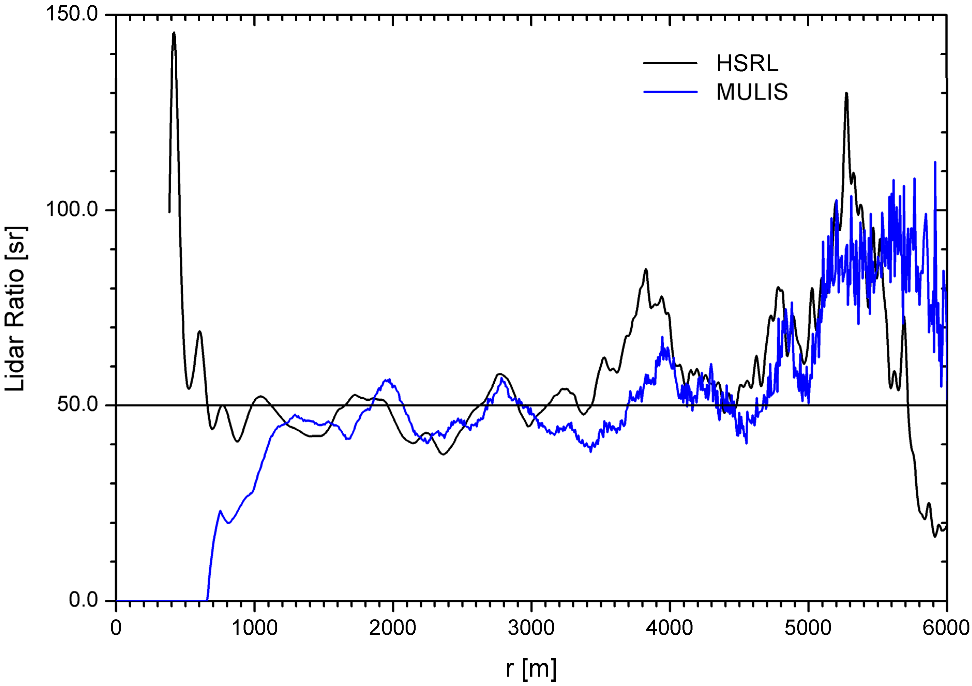

Fig. 13. 532.2-nm lidar ratios from the HSRL and MULIS: The performance of MULIS is better above 3.3 km which we ascribe to the issues with the transient digitizer module for the HSR channel in the range of low signal.

https://doi.org/10.5194/egusphere-2026-5567
Preprint. Discussion started: 29 September 2026

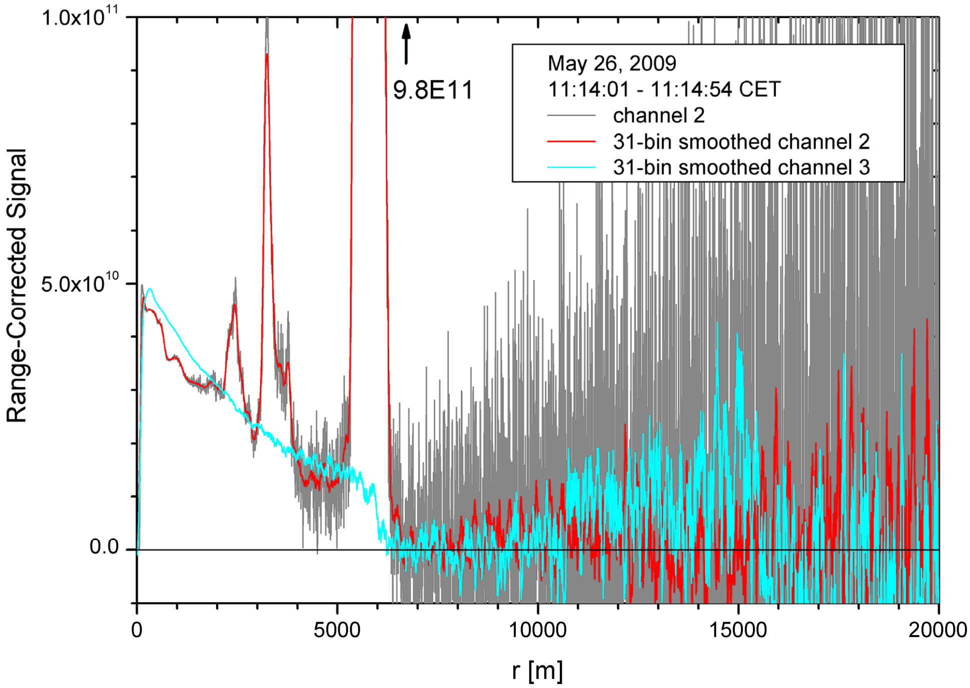

Fig. 14. 532.2-nm range-corrected signals from a 1-min measurement during the period of most pronounced clouds on 26 May, 2026; no signal correction beyond the small broad hump correction around 12.5 km was made. The read and cyan curves show ±15 bin sliding arithmetic averages. The pronounced digital structure in the HSR data (channel 3) can be seen above 10.7 km. No leak of the roughly 100 times stronger cirrus signal can be discerned.

https://doi.org/10.5194/egusphere-2026-5567
Preprint. Discussion started: 29 September 2026

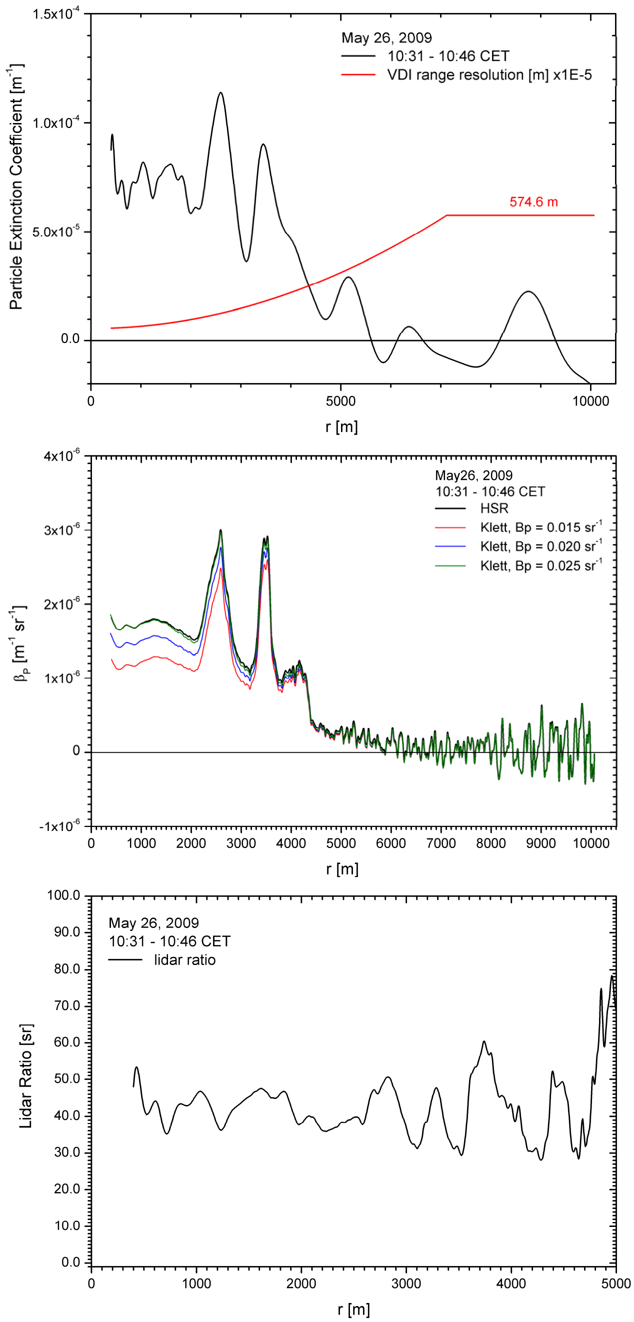

Fig. 15. 532.2-nm extinction coefficients, backscatter coefficients and lidar ratios for 15 summed subsequent measurements on 26 May 2009, between 10:31 and 10:46 CET. The lidar ratios look somewhat low, indicating a potential bias due to the technical limitations at that stage of the electronics.

https://doi.org/10.5194/egusphere-2026-5567
Preprint. Discussion started: 29 September 2026

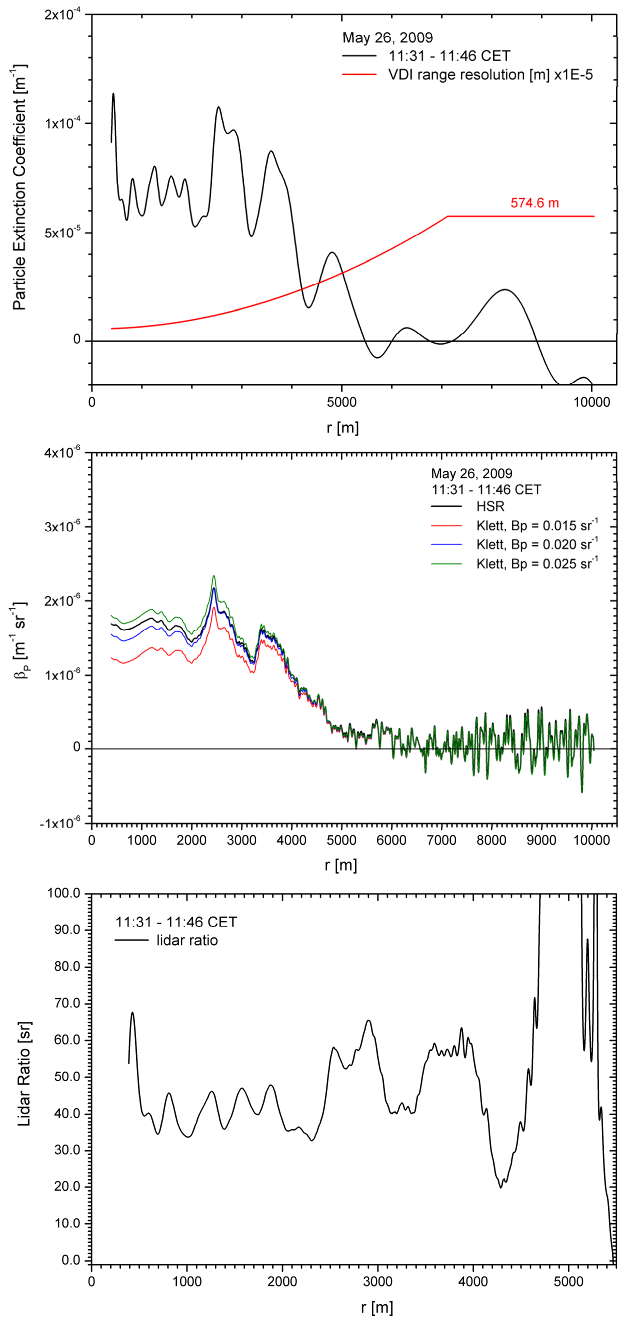

Fig. 16. 532.2-nm extinction coefficients, backscatter coefficients and lidar ratios for 15 summed subsequent measurements on 26 May 2009, between 11:31 and 11:46 CET. Because of the low extinction coefficients the values above 4 km become highly uncertain.

https://doi.org/10.5194/egusphere-2026-5567
Preprint. Discussion started: 29 September 2026

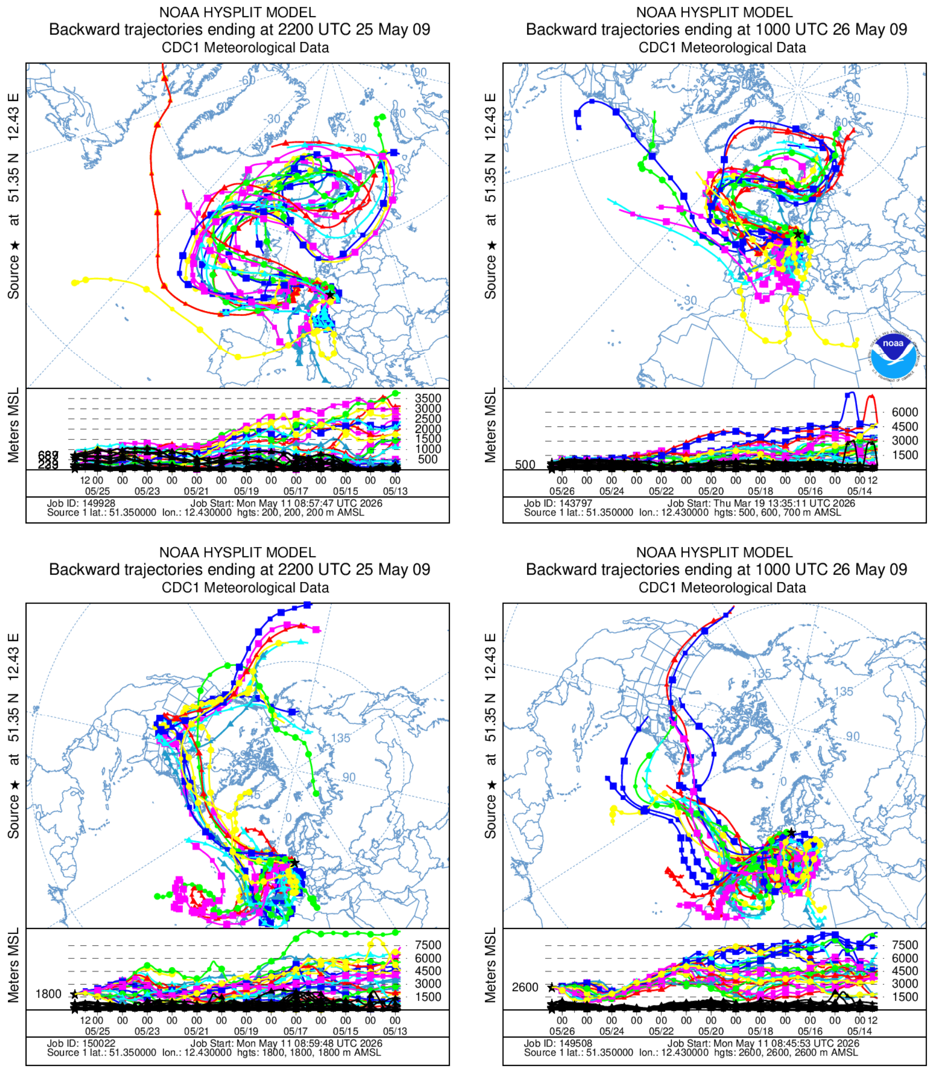

Fig. 17. HYPLIT 315 ensemble backward trajectories for 25 May 2009, 23:00 CET (left column), and 26 May 2009, 11:00 CET, (right column): At low altitudes (top row) now or low Saharan influence is seen within 315 h, within the pronounced aerosol layers (bottom row) the majority of the trajectories pass over the desert. The position of Leipzig is marked by black asterisks.